cmgh
CELLULAR AND MOLECULAR GASTROENTEROLOGY AND HEPATOLOGY

ORIGINAL RESEARCH

Loss of MYO5B in Mice Recapitulates Microvillus Inclusion Disease and Reveals an Apical Trafficking Pathway Distinct to Neonatal Duodenum

Victoria G. Weis,[1,2] Byron C. Knowles,[3,2] Eunyoung Choi,[1,2,4] Anna E. Goldstein,[1,2] Janice A. Williams,[1,2] Elizabeth H. Manning,[1,2,4] Joseph T. Roland,[1,2] Lynne A. Lapierre,[1,2,4] and James R. Goldenring[1,2,3,4]

[1]Department of Surgery, [2]Epithelial Biology Center, [3]Department of Cell and Developmental Biology, Vanderbilt University School of Medicine, [4]Nashville VA Medical Center, Nashville, Tennessee

SUMMARY

Three mouse models of MYO5B recapitulate the features of microvillus inclusion disease in neonatal mice, including the formation of inclusions and loss of apical transporters in the duodenum. The studies show the presence of a novel apical membrane internalization pathway in neonatal duodenal enterocytes.

BACKGROUND & AIMS: Inactivating mutations in myosin Vb (MYO5B) cause severe neonatal diarrhea in microvillus inclusion disease. Loss of active MYO5B causes the formation of pathognomonic inclusions and aberrations in brush-border enzymes.

METHODS: We developed 3 mouse models of germline, constitutively intestinal targeted, and inducible intestinal targeted deletion of MYO5B. The mice were evaluated for enterocyte cellular morphology.

RESULTS: Germline MYO5B knockout mice showed early diarrhea and failure to thrive with evident microvillus inclusions and loss of apical transporters in the duodenum. IgG was present within inclusions. Apical transporters were lost and inclusions were present in the duodenum, but were nearly absent in the ileum. VillinCre;MYO5B$^{F/F}$ mice showed similar pathology and morphologic changes in duodenal enterocytes. In contrast, when MYO5B KO was induced with tamoxifen treatment at 8 weeks of age, VillinCre^{ERT2};MYO5B$^{F/F}$ mice developed severe diarrhea with loss of duodenal brush-border enzymes, but few inclusions were observed in enterocytes. However, if tamoxifen was administered to 2-day-old VillinCre^{ERT2};MYO5B$^{F/F}$ mice, prominent microvillus inclusions were observed.

CONCLUSIONS: The microvillus inclusions that develop after MYO5B loss show the presence of an unrecognized apical membrane trafficking pathway in neonatal duodenal enterocytes. However, the diarrheal pathology after MYO5B loss is caused by deficits in transporter presentation at the apical membrane in duodenal enterocytes. *(Cell Mol Gastroenterol Hepatol 2016;2:131–157; http://dx.doi.org/10.1016/j.jcmgh.2015.11.009)*

Keywords: Enterocyte Trafficking; Brush Border; Rab11a; Rab8a; Syntaxin 3; NHE3; MYO5B.

Microvillus inclusion disease (MVID) is caused by inactivating mutations in myosin Vb (MYO5B).[1–3] Neonates with MVID have severe life-threatening diarrhea usually beginning in the first week of life.[4,5] Recent studies using in vitro investigations in correlation with human patient pathologic tissues have shown insights into the possible pathophysiology of MVID.[6–9] Our investigations have shown that MYO5B interactions with Rab8a are responsible for deficits in microvillar structure and trafficking, whereas interactions between MYO5B and Rab11a are responsible for microvillus inclusion formation.[9] Importantly, we were able to show that microvillus inclusions developed as a result of apical macropinocytosis.[9] Although in vitro studies using MYO5B knockdown and rescue in CaCo2 and CaCo2-BBE cells have identified important mechanisms that putatively are involved in MVID pathogenesis,[3,7–9] important questions remain about the significance of microvillus inclusions to the diarrhea phenotype and possible implications for treatment.

A recent publication reported a gene trap MYO5B knockout mouse that showed duodenal microvillus inclusions, but the pups died within 12 hours of birth, limiting the pathology analysis.[10] In addition, an inducible intestinal MYO5B knockout mouse recently was reported to develop microvillus inclusions within 4 days of MYO5B loss.[11] However, the sole reliance on adult mice to study a neonatal disease may hamper direct interpretation of the neonatal mechanisms involved in MVID. We now have developed germline, intestinally targeted, and inducible intestinal MYO5B knockout mice. Both germline MYO5B knockout mice and VillinCre;MYO5B$^{F/F}$ mice showed numerous microvillus inclusions in the proximal intestine,

Abbreviations used in this paper: ATPase, adenosine triphosphatase; DPPIV, dipeptidyl peptidase-4; E, embryonic day; KO, knockout; MYO5B, myosin Vb; MVID, microvillus inclusion disease; NHE3, sodium-hydrogen exchanger 3 protein; PCR, polymerase chain reaction; pERM, phosphorylated ezrin-radixin-moesin; SEM, scanning electron microscopy; TEM, transmission electron microscopy.

Most current article

2352-345X
http://dx.doi.org/10.1016/j.jcmgh.2015.11.009

but showed few inclusions in the distal small bowel. Inclusions contained IgG, suggesting their derivation from apical macropinocytosis involved with internalization of IgG from maternal milk. However, although 8-week-old Villin-Cre^{ERT2};MYO5B$^{F/F}$ mice induced with a single dose of tamoxifen developed severe diarrhea within 48 hours, they showed few microvillus inclusions. Nevertheless, if 2-day-old VillinCre^{ERT2};MYO5B$^{F/F}$ mice received tamoxifen, they developed prominent microvillus inclusions within 3 days. Diarrhea in all 3 mouse models was well correlated with losses in apical transporters in the proximal small intestine. These results show that microvillus inclusions in MYO5B knockout mice are not directly pathologic, but rather show the presence of a specialized apical membrane processing pathway in duodenal enterocytes during the neonatal period. The predominance of pathology in the proximal small intestine suggests that interventions promoting distal intestinal adaptation may represent an important strategy in the treatment of MVID neonates.

Materials and Methods

All authors had access to the study data and reviewed and approved the final manuscript.

Construction and Validation of MYO5B Deletion Mice

Embryonic stem cells harboring a knockout first allele for MYO5B (Figure 1*A*) were obtained from the Knockout Mouse Project (KOMP, Davis, CA). Embryonic stem cells (CSD78985 clone B10) were injected into C57BL/6 mouse blastocysts by the Vanderbilt Stem Cell Shared Resource. Ten chimeric male mice (50%–80% chimeric) were produced and mated with albino C57BL/6 mice to produce chimeric founders. One chimera was responsible for germline transmission to black offspring. The heterozygous mice from this line were mated for 1 year and produced no viable homozygous offspring. The mice therefore were crossed onto CD1 mice and after 3 generations crossed heterozygous mice gave birth to viable homozygous knockout offspring.

To produce floxed allele mice, the MYO5B$^{+/-}$ mice were bred with actin-FLP mice to derive MYO5B$^{flox/+}$ mice (Figure 1*A*). The MYO5B$^{flox/+}$ heterozygotes were crossed to produce homozygous MYO5B$^{flox/flox}$ mice (MYO5B$^{F/F}$). The MYO5B$^{F/F}$ mice then were crossed with both VillinCre and VillinCre^{ERT2} mice to produce VillinCre;MYO5B$^{F/F}$ targeted intestinal MYO5B deletion mice and VillinCre^{ERT2};MYO5B$^{F/F}$ inducible intestinal knockout mice. The care, maintenance, and treatment of animals in these studies followed protocols approved by the Institutional Animal Care and Use Committee of Vanderbilt University.

DNA was isolated from mice tails using the DNeasy Blood & Tissue Kit (Qiagen, Valencia, CA) according to the manufacturer's instructions. All genotyping was confirmed by specific polymerase chain reaction (PCR) with GoTaq Green Master Mix (Promega, Madison, WI) (Figure 1*B*) using the following PCR primer pairs: for Myo5B: MYO5BKO-F2, 5'-CTTGAGTTTGTTTAGTCTCTTGTCCCCTTTG-3' and MYO5B KO-R3, 5'-CCGCTGACTATGATGGATTGGTTCTTTTC-3'; for

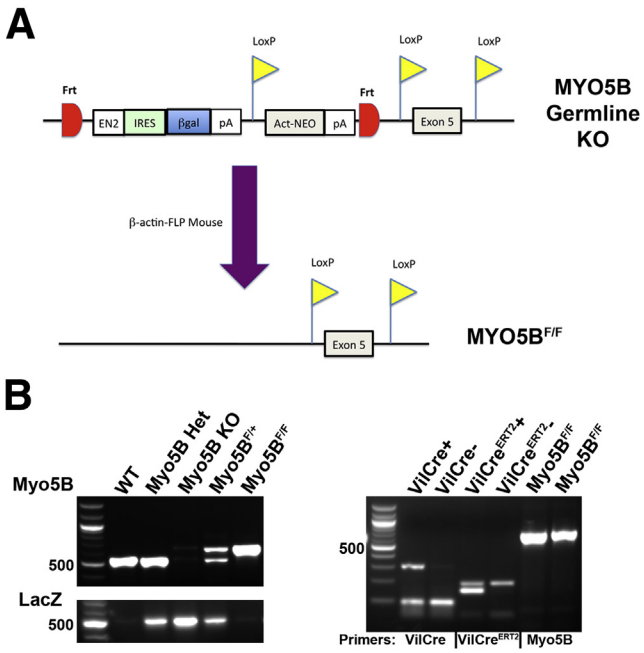

Figure 1. Generation of germline MYO5B KO and MYO5B$^{F/F}$ mice. (*A*) Schematic representation of the knockout first allele for MYO5B from the Knockout Mouse Project is shown. This construct was used to generate germline MYO5B KO mice by early termination of the Myo5B transcription before exon 5. Mice harboring this allele were mated to β-actin–FLP mice to also create MYO5B$^{F/F}$ mice in which LoxP sites flank exon 5. (*B*) PCR of genomic DNA shows the different PCR product patterns used to identify the genotype of a mouse. The 100-bp DNA Ladder (New England Biolabs, Ipswich, MA) is shown in the *left lane* of gels to denote PCR product size. The 500-bp marker is indicated.

LacZ: LacZ-1, 5'-TGCCGCTCATCCGCCACAT-3' and LacZ-2, 5'-CACCGATCGCCCTTCCCAACAGT-3'; for VillinCre: 16775, 5'-GCCTTCTCCTCTAGGCTCGT-3', 16776, 5'-TATAGGGCA-GAGCTGGAGGA-3', and oIMR9074, 5'-AGGCAAATTTTGGTG-TACGG-3'; and for VillinCre^{ERT2}: 5'Cre, 5'-CGCGAACATCTT CAGGTTCT-3' and 3'Cre, 5'-CAAGCCTGGCTCGACGGCC-3'. The following cycling parameters were used for Myo5B: 95°C (3 min), 95°C (30 s), 64°C (30 s), 72°C (45 s), and 72°C (5 min) with steps 2–4 repeated for 35 cycles. For LacZ and VillinCre PCR, the annealing temperature of 62°C was used, and VillinCre^{ERT2} PCR used 58°C.

For validation of Myo5B messenger RNA loss, total RNA was extracted from frozen duodenum samples using TRIzol (Invitrogen, Carlsbad, CA). Total RNA (1 μg) was treated with RQ1 RNase-free DNase (Promega), and then reverse-transcribed using Superscript III reverse transcriptase (Invitrogen) according to the manufacturer's instructions. PCR then was performed with Advantage Taq (Clontech, Mountain View, CA) using the following primers: exon 4: sense, 5'-CCTACGAGCAGCTGCCAATCTAC-3' and exon 5: antisense, 5'-GACACCGTCTTGCCTGCTCCAGACTCTC-3'. Cycling was performed at 95°C for 15 seconds and at 68°C for 20 seconds, for 42 cycles.

Western Blot Analysis

Fresh duodenum from each mouse was placed in 65°C lysis buffer (60 mmol/L Tris, pH approximately 6.8/10 mmol/L EDTA/2% sodium dodecyl sulfate) directly after euthanization. Samples were heated at 65°C for 10 minutes and then spun down for 10 minutes at 3600 rpm at 4°C. Samples were stored at -80°C until time of use. At time of Western blot, dithiothreitol (final concentration, 0.12 mmol/L) was added to each sample (50 μg of total protein), followed by 10 minutes of incubation at 65°C. Samples were resolved on a 4%–12% gradient Novex Bis-Tris gel (Invitrogen), and electrophoretically transferred onto Odyssey nitrocellulose membranes (Li-Cor, Lincoln, NE). Membranes subsequently were dried for 1 hour at room temperature, followed by blocking with Odyssey TBS blocking buffer (Li-Cor) for 1 hour at room temperature. Primary (rabbit anti-MYO5B, 1:500, Prestige cat. HPA040902; Sigma, St. Louis, MO; and rabbit anti-VDAC1/porin, 1:1000, cat. ab15895; Abcam, Cambridge, MA) and secondary antibodies (IRDye 800CW donkey anti-rabbit IgG, 1:15000, cat. 925-32213; Li-Cor) were diluted in the blocking buffer with 0.2% Tween-20. Membranes were visualized using the Odyssey Fc Imaging System (Li-Cor).

Determination of Mouse Weight and Stool Water Content

Mice from all 3 mouse models were weighed at time of euthanasia (at least n = 3 for each group). To determine stool water content, stool samples collected from the colon (3 control mice and 3 MYO5B mice) were placed in preweighed tubes and then the total stool weight was determined. The samples then were desiccated to dryness in a Speedvac (Thermo Savant, Pittsburgh, PA) and the tubes were reweighed. The differences in sample weights before and after desiccation were determined and used to determine the percentage of stool water. Comparisons were performed using a 1-tailed Mann–Whitney *U* test (Prism; GraphPad, La Jolla, CA) with a *P* value of .05 or less.

Induction of VillinCre^{ERT2};MYO5B$^{F/F}$ Mice With Tamoxifen

Cre recombinase was activated in 8- to 10-week-old VillinCre^{ERT2};MYO5B$^{F/F}$ mice (n = 9) by one intraperitoneal injection of tamoxifen (2 mg). Mice were killed 3 days after the tamoxifen dose. Tamoxifen-injected MYO5B$^{F/F}$ mice and VillinCre^{ERT2};MYO5B$^{F/+}$ mice (n = 8) were used as controls because no difference was found between induced MYO5B$^{F/F}$ and induced VillinCre^{ERT2};MYO5B$^{F/+}$ mice. For Cre recombinase activation in neonatal mice, 2-day-old VillinCre^{ERT2};MYO5B$^{F/+}$ (controls, n = 6) and VillinCre^{ERT2};MYO5B$^{F/F}$ (n = 4) littermates were given subcutaneous injections of tamoxifen (0.5 mg/g/day) for 2 consecutive days and killed 3 days after the first tamoxifen injection.

Immunofluorescence

For MYO5B knockout (KO) and VillinCre;MYO5B$^{F/F}$ mice, pups were euthanized between 2 and 8 days of age. Excised intestines were fixed in 4% paraformaldehyde overnight at 4°C and embedded in paraffin. Sections were deparaffinized and rehydrated before antigen retrieval was performed using Target Retrieval solution (DakoCytomation, Glostrup, Denmark) in a pressure cooker for 15 minutes. After cool down on ice, sections were blocked with the Mouse on Mouse Basic Kit (Vector Laboratories, Burlingame, CA) for 20 minutes at room temperature (except for mouse IgG staining), followed by protein block serum-free (Dako) for either 1 hour at room temperature or overnight at 4°C. The following primary antibodies were incubated at 4°C overnight: chicken anti-MYO5B (1:200),[9,12] rabbit anti-ezrin (1:200, cat. 3145; Cell Signaling, Danvers, MA), goat anti–dipeptidyl peptidase-4 (DPPIV) (1:200, cat. AF954; R&D Systems, Minneapolis, MN), mouse anti-CD10 (1:100, cat. ab47721; Abcam), mouse anti-CD10 (1:60, cat. 10R-CD10aHU; Fitzgerald, Acton, MA) (used for VillinCre^{ERT2};MYO5B$^{F/F}$ neonate studies), rat anti-Lamp2 (1:200, cat. ab13524; Abcam), rabbit anti-Rab8a (1:200),[9,13] rabbit anti-Rab11a (1:200, cat. R0009; US Biological Life Sciences, Salem, MA), rabbit anti-syntaxin 3 (STX3; 1:200, cat. ab4113; Abcam), rabbit anti–sodium-hydrogen exchanger 3 protein (NHE3) (1:200, a gift from Dr F. Ghishan, University of Arizona, Phoenix, AZ), rabbit anti–phosphorylated ezrin-radixin-moesin (pERM) (1:200, cat. 3149; Cell Signaling), mouse anti–E-cadherin (1:200, cat. 610181; BD Biosciences, Franklin Lakes, NJ), mouse anti-p120 (1:200, cat. 610133; BD Biosciences), mouse anti–Na/K–adenosine triphosphatase (ATPase) (1:50, cat. 05-369; Millipore, Billerica, MA), rabbit antilysozyme (1:2000, cat. ab108508; Abcam), rabbit anti-Muc2 (1:200, cat. sc-15334; Santa Cruz, Dallas, TX), rabbit anti-Chga (1:100, cat. ab17064; Abcam), and rabbit anti-villin (1:100, cat. R814; Cell Signaling). After 3 washes in 1× phosphate-buffered saline for 5 minutes each, sections were incubated for 1 hour at room temperature with the appropriate secondary antibodies conjugated for immunofluorescence with Alexa Fluor 488, Alexa Fluor 647, Cy2, Cy3, Cy5, or Cy7 (1:500; Molecular Probes, Eugene, OR; or Jackson ImmunoResearch, West Grove, PA). For Ki67 immunofluorescence, sections were incubated with directly conjugated anti-Ki67–Alexa Fluor 647 (1:50, cat. 652408; BioLegend) at the same time as the secondary antibodies. Slides then were washed 3 times with 1× phosphate-buffered saline and mounted with ProLong Gold Antifade Reagent with 4′,6-diamidino-2-phenylindole (Invitrogen). For mouse IgG immunofluorescence, sections were incubated with goat anti-mouse IgG (H+L) Alexa Fluor 488 (cat. A11029; Molecular Probes) at the time of primary antibody incubation. This signal then was amplified by incubation with donkey anti-goat Alexa Fluor 488 (cat. A11055; Molecular Probes) at the time of secondary antibody incubation. All sections were analyzed using Zeiss Axiophot microscope equipped with an Axiovision digital imaging system (Zeiss, Jena GmBH, Germany) or an Olympus FV1000 confocal microscope (Tokyo, Japan).

Quantitation of Fused Villi, Inclusions, Proliferation, and Paneth Cells

For quantitation of fused villi and inclusions, slides immunostained with the appropriate antibodies were scanned

using the Ariol SL-50 automated slide scanner (Genetix, San Jose, CA). Three randomly selected sections of well-oriented duodenum and ileum were selected for quantitation. A total approximate intestinal length of 1.5 mm (for MYO5B KO), 2 mm (for VillinCre;MYO5B$^{F/F}$), or 2.5–3.5 mm (for Villin-Cre^{ERT2};MYO5B$^{F/F}$) was quantified per mouse (n = 3) from both the duodenum and the ileum for fused villi and inclusions. For fused villi quantitation, a villus structure was considered fused if the apical membrane of a villus was observed on exiting the crypt (as marked by ezrin immunostaining), but later was lost in conjunction with a neighboring villus. For example, if 2 separate villi with marked apical membranes emerged from crypts but later converged and lost sections of apical membrane accompanied by obvious interconnected cells (as marked on the basolateral membrane by p120 immunostaining), 2 fused villi were counted. For comparisons, the total number of fused villi then was normalized by the linear length of intestine quantified.

The same regions of tissue used for fused villi quantitation were used for quantification of inclusions. Inclusions were identified as being round internal ezrin-positive structures (obvious deep invaginations from the apical membrane not normally found in controls also were included as inclusions). The total number of inclusions was quantified as the total counted number of ezrin-positive inclusions normalized by the total linear length of tissue examined. For co-labeled inclusions, these same regions were examined for ezrin and CD10 or ezrin and DPPIV co-labeled inclusions. All ezrin-positive inclusions identified for the total inclusion quantitation were examined for co-labeling with either CD10 or DPPIV. The number of dual-labeled inclusions was presented as the percentage of the total ezrin-positive inclusions that co-labeled with CD10 or DPPIV.

For quantitation of proliferation and presence of Paneth cells, sections immunostained for either Ki67 (proliferation) or lysozyme (Paneth cells) were analyzed. Two regions of randomly selected, well-oriented crypts from the duodenum of each mouse (n = 3 for each group) were examined for the total number of Ki67-positive cells. At least 5 crypts from each mouse were quantified. The total number of Ki67-positive cells was normalized by the number of crypts counted to obtain the average number of proliferating cells per crypt. The early maturation of Paneth cells in neonatal mice was quantified by lysozyme immunostaining. Again, 2 regions of randomly selected, well-oriented crypts (for 5–10 crypts total) from the duodenum of each mouse (n = 3) were quantified for the number of lysozyme-positive cells. The total number of lysozyme-positive cells was normalized by the number of crypts counted. All comparisons were performed using a 1-tailed Mann–Whitney *U* test (GraphPad Prism) with a significant *P* value of .05 or less.

Electron Microscopy

For transmission electron microscopy (TEM) and scanning electron microscopy (SEM) preparation, freshly excised duodenum tissue was washed quickly in 0.1 mol/L cacodylate buffer. Samples then were fixed in 2.5% glutaraldehyde (in 0.1 mol/L sodium phosphate buffer, pH 7.4, 0.1 mol/L cacodylate buffer) for 30 minutes at room temperature followed by overnight fixation at 4°C. After washing, samples were treated with 1% osmium tetroxide for 1 hour and dehydrated through serial ethanol dilutions (30%, 50%, 70%, 95%, and 100%). For SEM, after ethanol dehydration, samples were incubated with hexamethyldisilazane, mounted on stubs, and coated with gold in a sputter coater. Images were obtained using an FEI Quanta 250 scanning electron microscope (Hillsboro, OR). For TEM, tissue was incubated with propylene oxide followed by removal of ethanol from the samples before infiltration with and embedding in EPON 812 resin (Electron Microscopy Sciences, Hatfield, PA). Ultrathin sections (70- to 80-nm thick) were cut and collected on 300-mesh copper grids. Sections were stained with 2% uranyl acetate and then Reynold's lead citrate. Images were obtained using a Philips/FEI T-12 Tecnai T12 electron microscope (Hillsboro, OR). For quantification of microvilli length and width, TEM images were evaluated for at least 60 microvilli from each mouse using an AMT Image Capture Engine (Woburn, MA) to analyze images obtained with a DVC camera (Austin, TX). Statistical differences were determined using a 1-tailed Mann–Whitney *U* test (GraphPad Prism) with a significant *P* value of .05 or less.

Results

MYO5B Germline KO Mice Display Failure to Thrive, Aberrant Villi Structure, and Microvillus Inclusions

Breeding of C57BL/6 MYO5B heterozygous mice did not yield any viable MYO5B KO pups after 1 year of breeding, thus C57BL/6 MYO5B heterozygous mice were crossed onto the outbred CD1 background. After 3 generations, viable C57BL/6;CD1 germline MYO5B KO pups were obtained. Analysis of MYO5B by PCR and Western blot confirmed the loss of MYO5B messenger RNA and protein (Figure 2*A* and *B*). Furthermore, immunofluorescence for MYO5B showed loss of MYO5B from the intestine of MYO5B KO mice (Figure 2*C*). Although MYO5B KO mice were indistinguishable from both wild-type and heterozygous littermates at birth, by 3 days old, MYO5B KO mice had a significantly higher percentage of water in their stool (Figure 2*D*). By 5 days old, MYO5B KO mice were visibly smaller and weighed significantly less than both wild-type and heterozygous littermates (Figure 2*E* and *F*). No differences in weight or pathology were seen between wild-type and heterozygous MYO5B mice, so both were used as controls in further studies. Of note, colon and liver histology in MYO5B KO mice appeared predominately normal, so further studies focused on the small intestine.

In control duodenum, ezrin immunostained the microvilli on the apical surface of enterocytes along the villi (Figure 3*A*). In MYO5B KO duodenum, ezrin immunostaining showed fused villi (Figure 3*A*) with approximately 8 fused villi per 500-μm length of duodenum (Figure 4*C*). Previous studies have noted villus fusion in MVID patients[14] as well as in ezrin KO mice.[15] In addition, we observed intracellular ezrin-positive inclusions (Figure 3*A*) at a prevalence of 140 inclusions per 500-

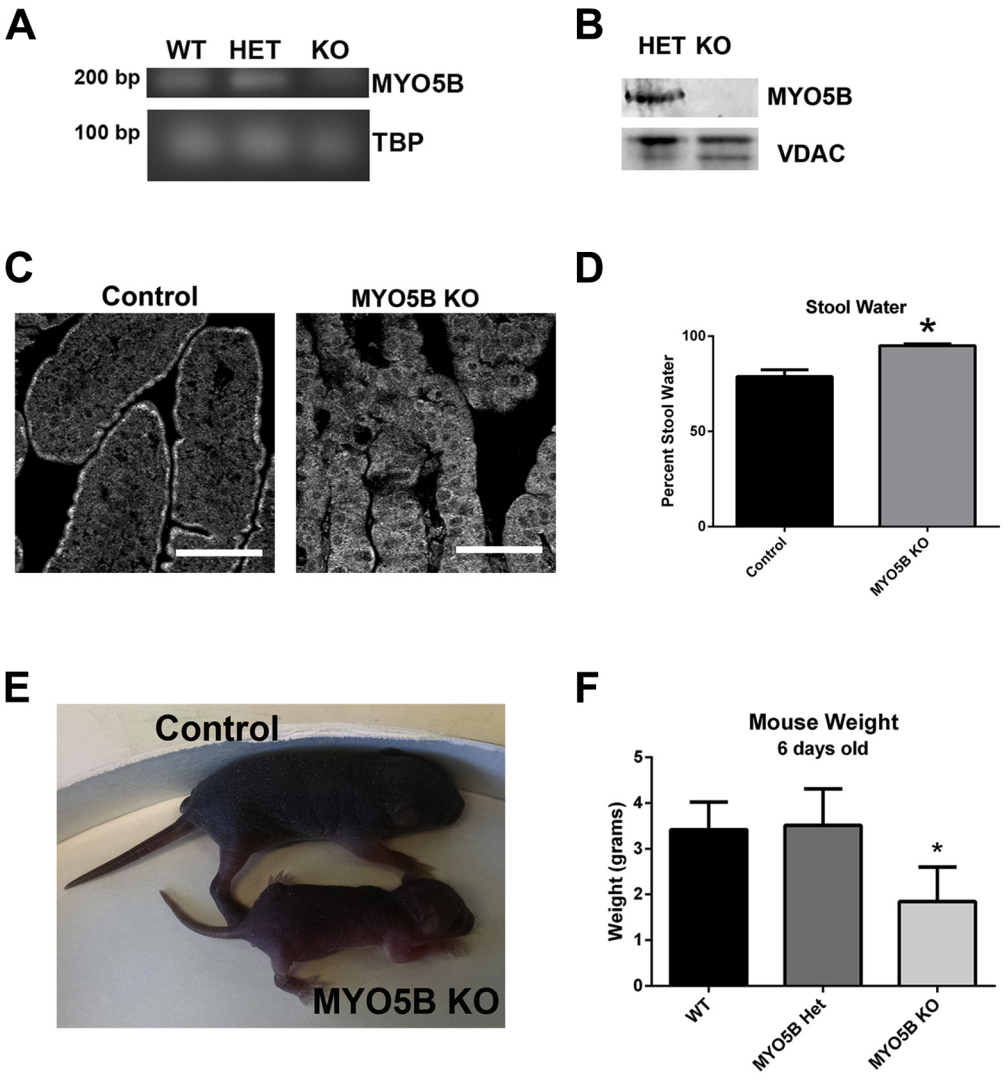

Figure 2. Germline MYO5B KO mice fail to thrive. (*A*) PCR of complementary DNA from wild-type (WT), MYO5B Het, and MYO5B KO mouse duodenum confirmed Myo5B messenger RNA loss. Tata-box binding protein (TBP) was used as a loading control. (*B*) Western blot of duodenum confirms MYO5B protein loss in a MYO5B germline KO mouse as compared with a MYO5B heterozygote mouse. VDAC was used as a loading control. (*C*) Immunofluorescence for MYO5B in control duodenum shows subapical staining. This subapical staining was lost in MYO5B KO duodenum. *Scale bar*: 50 μm (*D*) The percentage of stool constituted by water was calculated in control and MYO5B KO mice (n = 3). MYO5B KO mice had significantly higher water content in stool collected from the colon. *$P = .05$. (*E*) Picture of control and MYO5B KO littermates at 5 days old shows the reduced size of MYO5B KO mice. (*F*) Mice weighed at 6 days old show no difference between WT and MYO5B Het mice. MYO5B KO mice were significantly smaller than control littermates (both WT and Het) (n=3). *$P = .05$.

μm length of duodenum (Figure 4*D*). The ezrin-positive inclusions typically were circular, with a diameter of 2–4 μm. The ezrin-positive inclusions appeared along the entire length of the villi beginning in cells just emerging from the crypts. To examine the effects of MYO5B loss on other enterocyte components previously shown as disrupted in MVID patients,[9,16] MYO5B KO duodenum was immunostained for DPPIV and CD10. In control proximal small intestine, DPPIV predominately labeled the apical surface with only a small amount of subapical DPPIV observed, and CD10 localized to the apical surface of enterocytes. In contrast, in MYO5B KO duodenum, a significant subapical localization of DPPIV was observed as well as localization in small punctate vesicles and ezrin-positive inclusions (Figure 3*B* and *C*). Similarly, CD10 was decreased markedly along the apical surface and also mislocalized to a subapical compartment and in ezrin-positive inclusions in MYO5B KO duodenum (Figure 3*B* and *C*). More than 98% of ezrin-positive inclusions co-labeled with CD10 and DPPIV (Figures 3*C* and 4*E*).

The proximal small intestine was compared with the distal small intestine in MYO5B KO mice to examine differences along the length of the small intestine. Ezrin labeled the apical surfaces along the villi of the control distal small intestine, outlining individual villi as seen in the control duodenum. Although MYO5B KO duodenum had numerous fused villi, ezrin immunostaining of the MYO5B

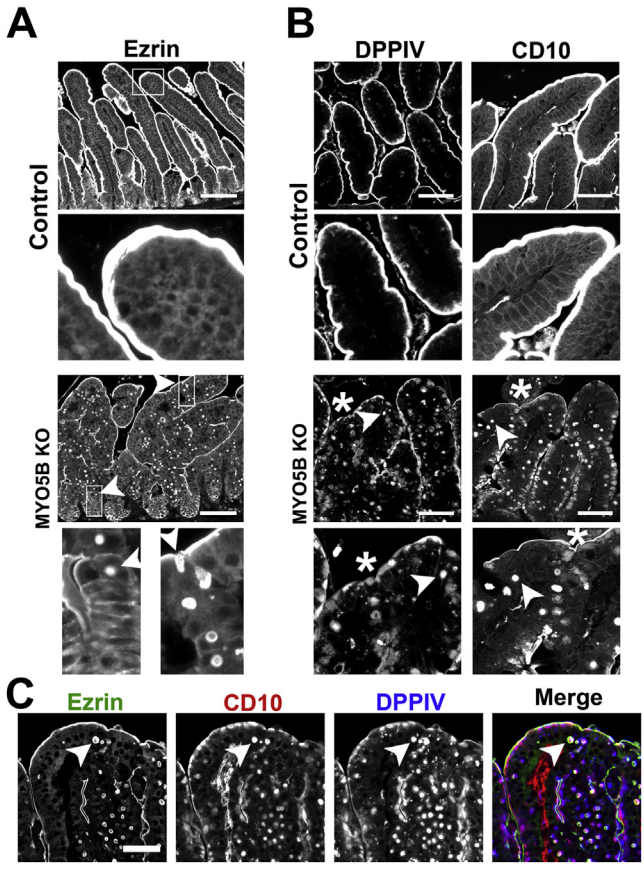

Figure 3. Immunofluorescence of MYO5B KO duodenum. (*A*) Ezrin immunostaining in control mice show a fully formed brush border along the length of single villi. The inset shows no internal ezrin staining. In MYO5B KO duodenum, ezrin labeled internal inclusions in addition to the apical brush border. *Left inset*: inclusions formed in cells just exiting the crypt (*arrowhead*). Inclusions also were found forming along the apical membrane (*arrowhead*, *right inset*). Ezrin immunostaining also showed fused villi in MYO5B KO duodenum. *Scale bar*: 100 μm. (*B*) DPPIV and CD10 both labeled the apical brush border in control mice with no internal structures labeled (*inset*). In MYO5B KO duodenum, DPPIV and CD10 was collapsed from the apical surface into a diffuse subapical localization (*) as well as localized to internal inclusions (*arrowheads*). DPPIV also was found localized to small punctate vesicles (DPPIV *inset*). *Scale bar*: 50 μm. (*C*) MYO5B duodenum immunostained for ezrin (green), CD10 (red), and DPPIV (blue) show ezrin-positive inclusions co-labeled with CD10 and DPPIV (*arrowhead*). *Scale bar*: 50 μm.

KO distal small intestine showed single villi similar to the controls (Figure 4*A* and *C*). Likewise, significantly fewer Ezrin-positive inclusions were observed in the distal small intestine than in the proximal intestine of MYO5B KO mice (Figure 4*A* and *D*). No inclusions were noted in the colonic mucosa of MYO5B KO mice (Figure 4*F*).

We next used DPPIV immunostaining to examine expression along the intestinal tract. CD10 expression was not used for distal small intestine analysis because we noted CD10 expression significantly decreases in normal murine distal small intestine (data not shown). In control distal small intestine, DPPIV labeled the apical surface as well as a small subapical compartment (Figure 4*B*). DPPIV immunostaining of MYO5B KO mouse distal small intestine showed few intracellular inclusions, similar to the ezrin immunostaining (Figure 4*B*). However, when ezrin-positive inclusions were observed in the distal intestine, they usually also stained for DPPIV (Figure 4*E*). In addition, in MYO5B KO intestine, the localization of DPPIV to small punctate vesicles in the duodenum was not observed in the distal small intestine (Figure 4*B*). These findings indicate that MYO5B loss induces a gradient of pathology along the length of the small intestine with the predominate pathology located in the proximal intestine.

To examine the ultrastructure of the inclusions found predominately in the duodenum, we performed TEM on duodenum from 7-day-old MYO5B KO mice. By TEM analysis, inclusions with microvilli were observed inside enterocytes (Figure 5). In addition, omega-shaped invaginations containing apical microvilli were observed at the apical surface. Thus, MYO5B germline KO mice developed microvillus inclusions, as seen in MVID patients.

In MYO5B knockdown Caco2-BBE cells, internalized DPPIV was trafficked to lysosomes.[9] To examine if the internal DPPIV punctate vesicles or the ezrin-positive microvillus inclusions were localized with lysosomes, we co-immunostained for DPPIV or ezrin with Lamp2. In control duodenum, Lamp2-positive lysosomes were located subapically just under the ezrin- and DPPIV-positive brush border (Figure 6*A* and *B*). In MYO5B KO duodenum, a subset of ezrin-positive inclusions were not localized near Lamp2-positive lysosomes, whereas other ezrin-positive inclusions appeared to be surrounded closely by, but not co-localized with, Lamp2-positive lysosomes (Figure 6*A*). Similarly, internal DPPIV found on microvillus inclusions did not co-localize with Lamp2 (Figure 6*B*). However, the DPPIV-positive punctate vesicles in KO duodenum co-labeled with Lamp2 suggests that a portion of the internalized DPPIV not found in ezrin-positive microvillus inclusions was diverted to lysosomes (Figure 6*B*).

Germline MYO5B Loss Disrupts Apical Trafficking But Not Microvilli Formation or Basolateral Protein Localization

To determine the effects of MYO5B loss on apical trafficking and polarity, we examined immunostaining for apical trafficking proteins (Rab8a, Rab11a, and STX3), the apical NHE3, and pERM, as a reflection of phosphorylated ezrin in microvilli. Recent studies have shown that loss of MYO5B results in dispersion of MYO5B binding proteins Rab8a and Rab11a.[9,11] In control duodenum, Rab8a and Rab11a were concentrated predominately in the subapical compartment (Figure 7). In MYO5B KO duodenum, Rab8a was decreased significantly from its normal subapical location and instead was localized to inclusions (Figure 7). In addition, normal Rab11a localization was lost and only occasional inclusions were labeled with Rab11a in MYO5B KO duodenum (Figure 7). Loss of Rab11a from enterocytes has been shown to alter the localization of the apical soluble NSF attachment protein receptor protein, STX3.[17] STX3 was limited to the

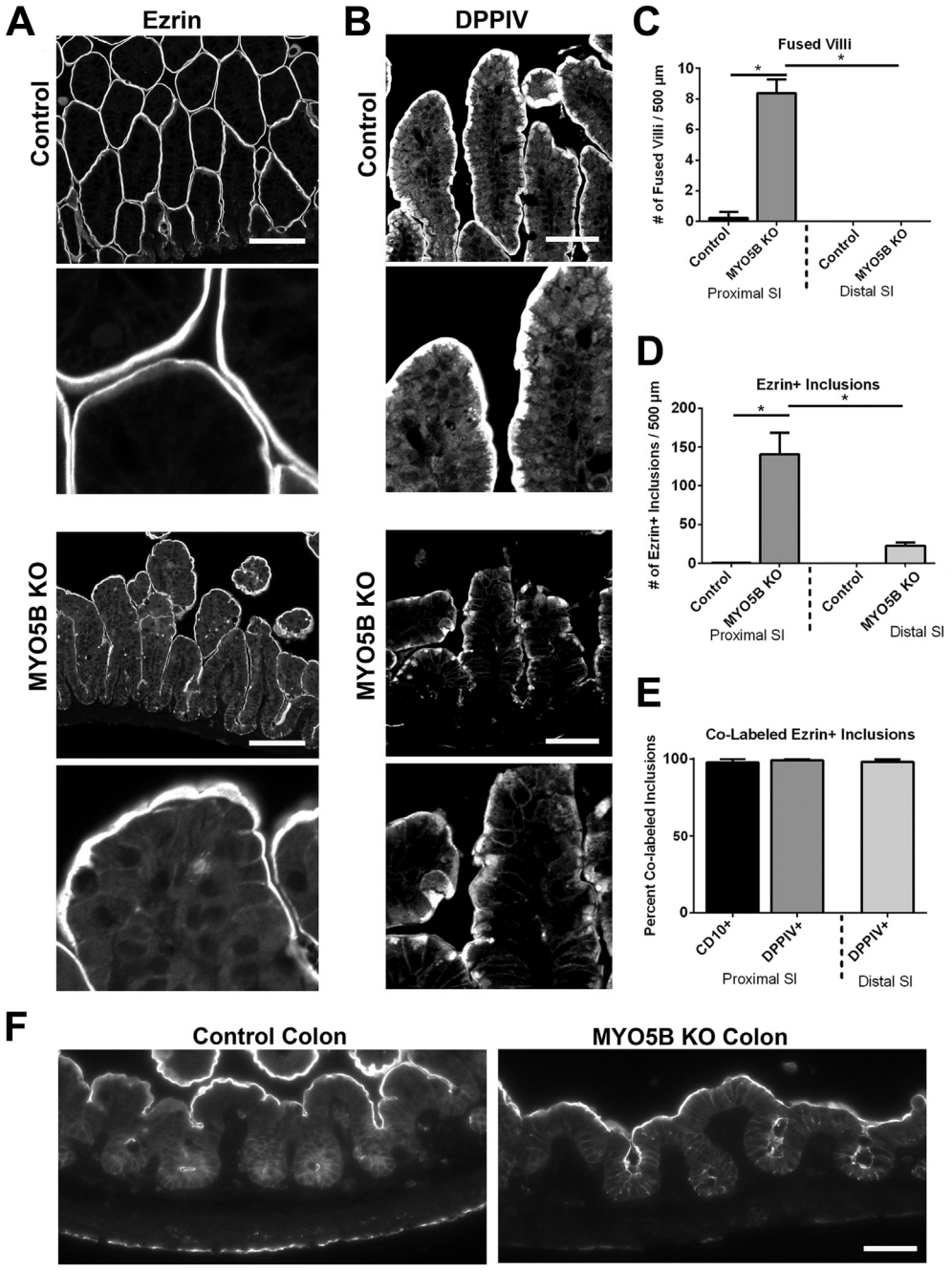

Figure 4. Comparison of distal small intestine and colon. (*A*) Distal small intestine from control and MYO5B KO mice was immunolabeled for ezrin. In control distal small intestine, ezrin labeled the apical brush border with no intracellular immunoreactivity, as found in the proximal intestine. Distal MYO5B KO small intestine showed only occasional fused villi and few ezrin-positive inclusions along with the apical membrane labeling. *Scale bar*: 100 μm. (*B*) In control distal small intestine, DPPIV labeled the apical membrane with a small subapical population. DPPIV localization in MYO5B KO distal small intestine appeared similar to control tissue with a compact subapical localization in addition to the apical membrane. In addition, fewer DPPIV-positive intracellular inclusions were found. *Scale bar*: 50 μm. (*C*) The number of fused villi was counted in both the proximal and distal intestine in control and MYO5B KO mice. MYO5B KO proximal intestine had approximately 8 fused villi per 500-μm length of intestine, which was increased significantly from the controls. A decreasing gradient in the number of fused villi was observed in MYO5B KO intestine with only rare fused villi found in the distal small intestine. $^*P = .05$. (*D*) MYO5B KO duodenum had approximately 140 ezrin-positive inclusions per 500 μm of intestine. Again, the number of inclusions was decreased significantly in MYO5B KO distal small intestine as compared with MYO5B KO duodenum. $^*P = .05$. (*E*) The percentage of ezrin-positive inclusions that co-labeled with CD10 or DPPIV was quantified. More than 98% of all ezrin-positive inclusions were dual-labeled with ezrin and CD10 or ezrin and DPPIV. No difference in co-labeled inclusions was found between the proximal and distal small intestine. (*F*) Colon from control and MYO5B KO mice was immunolabeled for ezrin. No microvillus inclusions were observed in MYO5B KO colon. *Scale bar*: 50 μm.

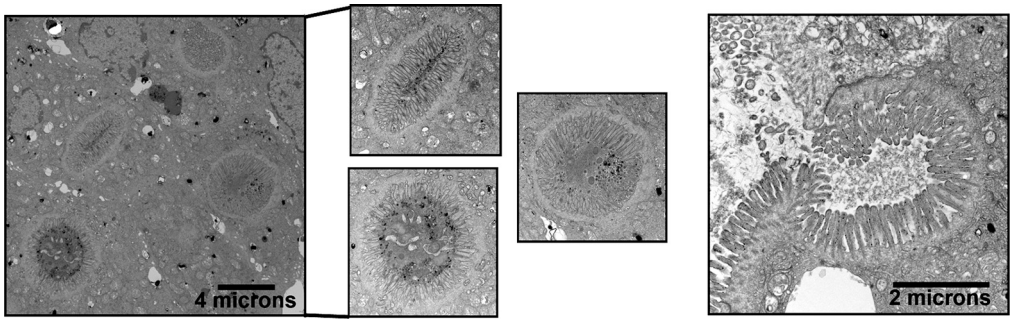

Figure 5. TEM identification of microvillus inclusions. TEM analysis of MYO5B KO duodenum showed inclusions with fully formed microvilli, confirming the formation of microvillus inclusions. Several microvillus inclusions were visualized within the enterocytes of the duodenum (*left four panels*). *Scale bar*: 4 μm. In addition, microvillus inclusion was visualized at the apical membrane with characteristic omega-shaped invaginations of the brush-border microvilli (*right panel*). *Scale bar*: 2 μm.

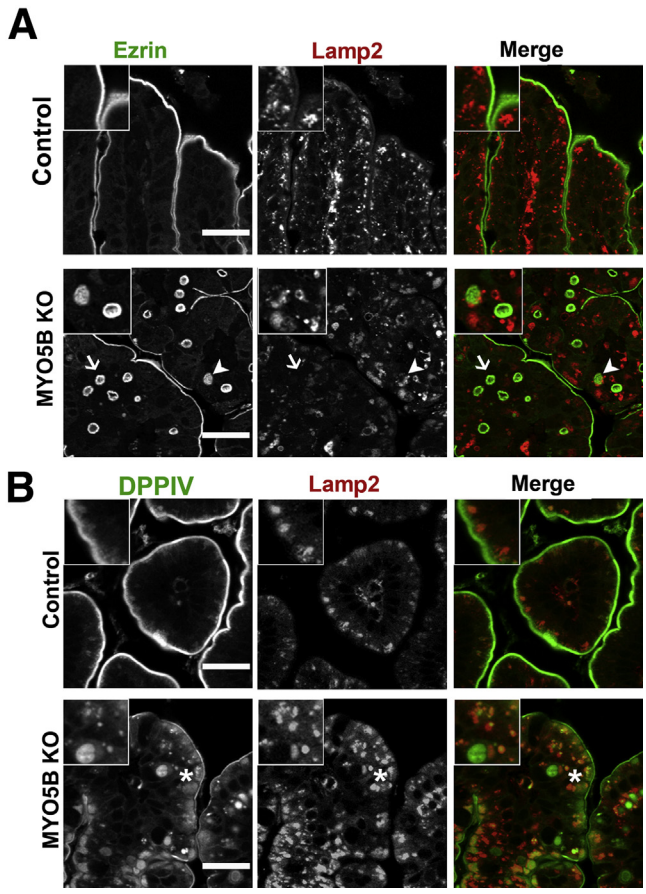

Figure 6. Trafficking of ezrin-positive inclusions and DPPIV. (*A*) Duodenum from control and MYO5B KO mice were co-stained for ezrin (green) and Lamp2 (red). In control enterocytes, Lamp2-positive lysosomes concentrated just under the apical surface. Upon MYO5B loss, a subset of ezrin-positive inclusions were surrounded closely or cupped by Lamp2-positive lysosomes (*arrowheads*). However, other ezrin-positive inclusions were not located near Lamp2 (*arrows*). *Scale bars*: 25 μm. (*B*) In controls, the small DPPIV population occasionally found in the subapical region co-localized with Lamp2. *In MYO5B KO duodenum, the subset of DPPIV that mistrafficked to small punctate vesicles was found to co-label with Lamp2. *Scale bars*: 25 μm.

subapical compartment in normal neonate duodenum. In MYO5B KO duodenum, STX3 was more dispersed into the cytoplasm as well as localized to some microvillus inclusions (Figure 7). Similar to the disruption of the apical trafficking proteins, the apical NHE3 also was mislocalized. Although NHE3 was found strictly on the apical membrane in normal duodenum, in MYO5B KO mice, NHE3 was collapsed into a diffuse subapical localization as well as localized in inclusions (Figure 7). To examine the effects of MYO5B loss on a structural component of the apical microvilli, we immunostained MYO5B KO intestine for pERM. Although the apical pERM localization was retained in MYO5B KO intestine, pERM also clearly labeled inclusions (Figure 7), further validating the presence of mature microvilli within the inclusions and suggesting the retention of apical microvilli on enterocytes along the villi.

To study the effects of MYO5B loss on basolateral trafficking, we immunostained for E-cadherin, p120, and Na/K-ATPase. All 3 proteins were found on the basolateral membrane in control duodenum. This basolateral localization was maintained in MYO5B KO duodenum (Figure 8). In addition, immunostaining of these 3 basolateral proteins highlighted the fusion of villi and the potential disorganization of enterocytes in these fused villi. This disorganization caused by villi fusion may confound the observation of subtle changes in basolateral trafficking. No changes were found for immunostaining of tight junction proteins (data not shown).

Although germline deletion of MYO5B led to a disruption and mislocalization of a number of apical trafficking proteins, ezrin and pERM staining suggest the presence of structurally intact apical microvilli in MYO5B KO mice. Thus, we performed TEM and SEM to assess the presence of apical microvilli in the enterocytes. TEM of control duodenum showed long, straight microvilli along the apical surface (Figure 9*A*). Apical microvilli were retained in MYO5B KO duodenum (Figure 9*B*). However, similar to the previously reported Rab11a KO mouse,[17,18] MYO5B KO duodenum showed significantly shortened and wider apical microvilli (Figure 9*B* and *C*). Although microvilli were shorter in comparison with control duodenum (Figure 9*D*), normal packing of microvilli was found in MYO5B KO duodenum (Figure 9*E*), suggesting

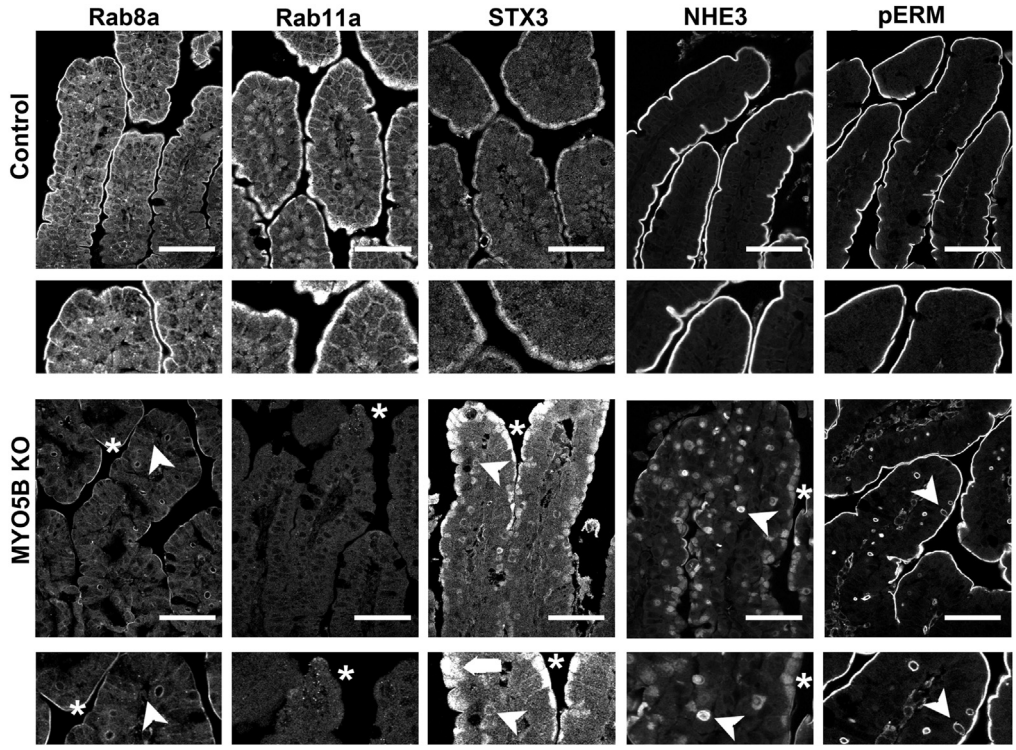

Figure 7. Disruption of apical trafficking in MYO5B KO duodenum. Control (*top row*) and MYO5B KO (*bottom row*) duodenal sections were immunostained for apical proteins (Rab8a, Rab11a, STX3, NHE3, and pERM). Apical trafficking proteins, Rab8a, Rab11a, and STX3, were concentrated subapically in control tissue, with Rab8a also labeling along lateral membranes. *Rab8a and Rab11a were lost from the apical membrane and occasionally localized to inclusions (*arrowheads*) in MYO5B KO duodenum. STX3 was collapsed into a broad and diffuse subapical region (*asterisks* and *arrowheads*), as well as localized to inclusions (*arrowheads*). The apical exchanger NHE3 was normally located on the apical membrane of enterocytes in the small intestine. Upon MYO5B loss, NHE3 was mislocalized to a diffuse subapical compartment (*asterisks*) and labels inclusions (*arrowheads*). In addition, a microvilli structural protein, pERM, was examined to further investigate the status of microvilli in MYO5B KO tissue. pERM in control duodenum labeled only on the apical surface of the villus enterocytes. As with ezrin, in MYO5B KO duodenum, pERM immunostaining identified microvillus inclusions inside enterocytes as well as the formation of microvillus inclusions at the apical surface of enterocytes (*arrowheads*). *Scale bars*: 50 μm.

that microvilli formation was not altered significantly upon loss of MYO5B in neonates.

Disruption of Apical Trafficking, But Not Microvillus Inclusion Formation, Is Present in Embryonic MYO5B KO Duodenum

We examined embryonic (embryonic day E18.5) duodenum from control and MYO5B KO littermates to determine the onset of the apical trafficking disruption and the formation of microvillus inclusions. Embryonic duodenum was immunostained for ezrin, DPPIV, CD10, and NHE3. Embryonic control duodenum showed strict apical localization of each marker (Figure 10), similar to that seen in neonatal control duodenum. Although neonatal MYO5B KO duodenum showed numerous ezrin-positive inclusions (beginning at 1 day old), E18.5 MYO5B KO duodenum did not possess ezrin-positive inclusions (Figure 10). However, mislocalization of the apical markers DPPIV, CD10, and NHE3 into a subapical compartment was observed in the embryonic KO duodenum (Figure 10).

Because previous studies have suggested that the duodenum is primed for maternal IgG uptake in neonatal rodents,[19–21] we dual immunostained for murine IgG and ezrin to assess the presence of maternal IgG inside the inclusions found in MYO5B KO neonates. Neonatal MYO5B KO duodenum sections were immunostained with an Alexa 488–conjugated goat anti-mouse IgG antibody to label native mouse IgG from maternal milk. No significant internal regions of concentrated IgG were found in control neonatal duodenum (Figure 11). In MYO5B KO duodenum, although not all inclusions immunostained for IgG, a prominent subset of ezrin-positive inclusions did co-label with murine IgG (Figure 11). These findings support the origin of microvillus inclusions through internalization of apical membrane.

Germline MYO5B Loss Leads to Crypt Hyperproliferation and Early Maturation of Paneth Cells

Because MYO5B loss results in aberrant villi structure, we examined the effects of MYO5B loss on proliferation and the cell lineages in the duodenum. Ki67 immunostaining showed a significant increase in proliferating cells within MYO5B KO crypts as compared with control crypts (12 vs 9 cells per crypt, respectively) (Figure 12*A* and *C*). No proliferating cells

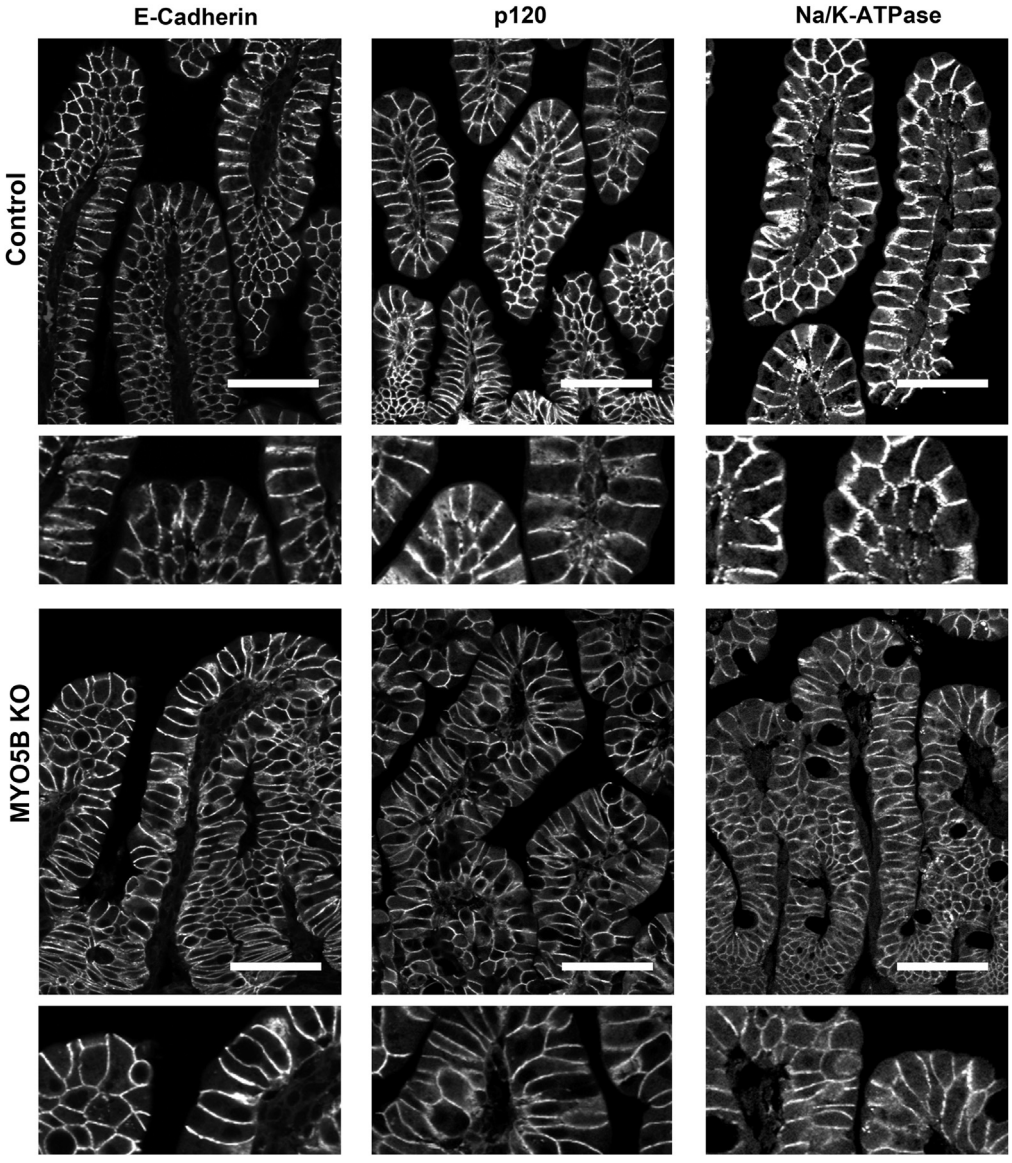

Figure 8. Immunofluorescence staining for basolateral trafficking. Duodenum sections were immunostained for junctional proteins E-cadherin and p120 and the basolateral Na/K-ATPase. All 3 proteins were localized to the basolateral membrane in control duodenum (*top row*). Similar basolateral localization was observed in MYO5B KO duodenum (*bottom row*), thus showing no disruption in basolateral trafficking upon MYO5B loss. *Scale bars*: 50 μm.

were observed outside of crypts in MYO5B KO duodenum. Lysozyme immunostaining was used to assess the presence of Paneth cells in the neonatal mice. Paneth cells do not normally mature in neonatal mice until 14 days of age.[22] Accordingly, in control duodenum, only rare lysozyme-positive Paneth cells were observed (Figure 12*B* and *C*). In MYO5B KO duodenum, early maturation of Paneth cells within the crypts was seen (Figure 12*B* and *C*). In contrast to the crypt, no significant differences were observed in the differentiation of secretory cell lineages along the villi, including enteroendocrine cells (labeled by chromogranin A) and goblet cells (labeled by Muc2) (Figure 12*D*).

Intestine-Targeted MYO5B Deletion in Mice Recapitulates the Pathology in Germline MYO5B KO Mice

To examine the role of MYO5B specifically in the intestine, we generated intestine-targeted MYO5B deletion mice by crossing VillinCre mice to MYO5B$^{F/F}$ to produce VillinCre;MYO5B$^{F/F}$ mice. In contrast to the germline MYO5B KO mice, viable VillinCre;MYO5B$^{F/F}$ pups were obtained on a C57BL/6 background. MYO5B immunostaining in intestinal sections confirmed loss of MYO5B along the length of the small intestine (Figure 13*A*) and colon (data not shown). Nevertheless, VillinCre;MYO5B$^{F/F}$ failed to thrive and did not survive past 6 days of age. Although indistinguishable from control littermates at birth, by 5 days of age, VillinCre;MYO5B$^{F/F}$ mice showed evidence of dehydration and were visibly smaller (Figure 13*B* and *C*). No differences in weight or pathology were observed between MYO5B$^{F/F}$ and VillinCre;MYO5B$^{F/+}$ mice, and thus both were used as controls in further studies.

Ezrin immunostaining in VillinCre;MYO5B$^{F/F}$ duodenum showed fused villi at a rate of 5.4 fused villi per 500-μm length of intestine (Figure 13*D* and *E*). In addition, ezrin-positive inclusions were found within the

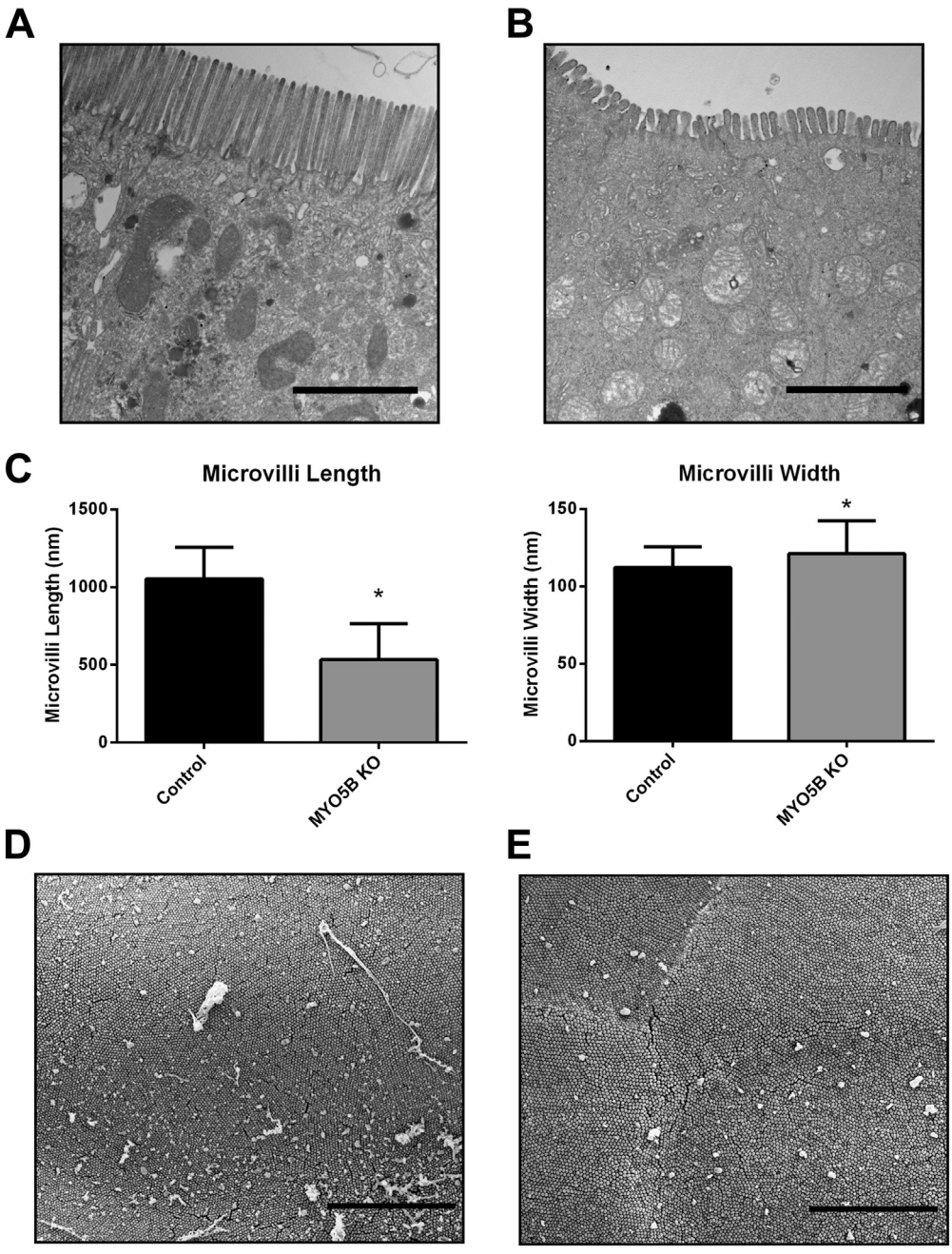

Figure 9. TEM and SEM analysis of apical microvilli. (*A*) Control duodenum was imaged by TEM. Images show long and straight microvilli on the apical surface of enterocytes. *Scale bar*: 2 μm. (*B*) TEM imaging of MYO5B KO duodenum showed shortened apical microvilli. *Scale bar*: 2 μm. (*C*) The length and width of apical microvilli from control and MYO5B KO duodenum was measured. In MYO5B KO duodenum, microvilli were half the height of control microvilli. In addition, microvilli were slightly wider in MYO5B KO duodenal enterocytes. *$P < .05$. (*D*) Control duodenum examined by SEM showed tightly packed microvilli. *Scale bar*: 5 μm. (*E*) By SEM, tightly packed microvilli were visualized in MYO5B KO duodenum, showing that packing remained largely unchanged even with shortened microvilli. *Scale bar*: 5 μm.

enterocytes along the villi in the proximal small intestine (averaging 82 ezrin-positive inclusions per 500-μm length of intestine) (Figure 13*D* and *E*). We then examined the number of fused villi and ezrin-positive inclusions in the distal small intestine of VillinCre;MYO5B$^{F/F}$ mice. Similar to MYO5B KO mice, a decreasing gradient was observed between the proximal and distal small intestine. Only rare fused villi were observed in the VillinCre;MYO5B$^{F/F}$ mouse distal small intestine and the presence of ezrin-positive inclusions was significantly less frequent (<5 ezrin-positive inclusions per 500-μm length of intestine) (Figure 13*D* and *E*). However, regardless of the location of the ezrin-positive inclusions (proximal vs distal), more than 97% of all ezrin-positive inclusions co-labeled with CD10 and DPPIV (Figure 13*E*).

VillinCre;MYO5B$^{F/F}$ Mice Show Disruption of Apical Trafficking, But Not Basolateral Protein Localization or Microvilli Formation

Although normal localization of pERM to the apical brush border was retained in VillinCre;MYO5B$^{F/F}$ mouse duodenum, pERM-positive inclusions also were observed in the cytoplasm of enterocytes along the villi (Figure 14*A*). Similar to the apical trafficking disruption found in germline MYO5B KO mice, strict apical localization of NHE3, CD10, and DPPIV

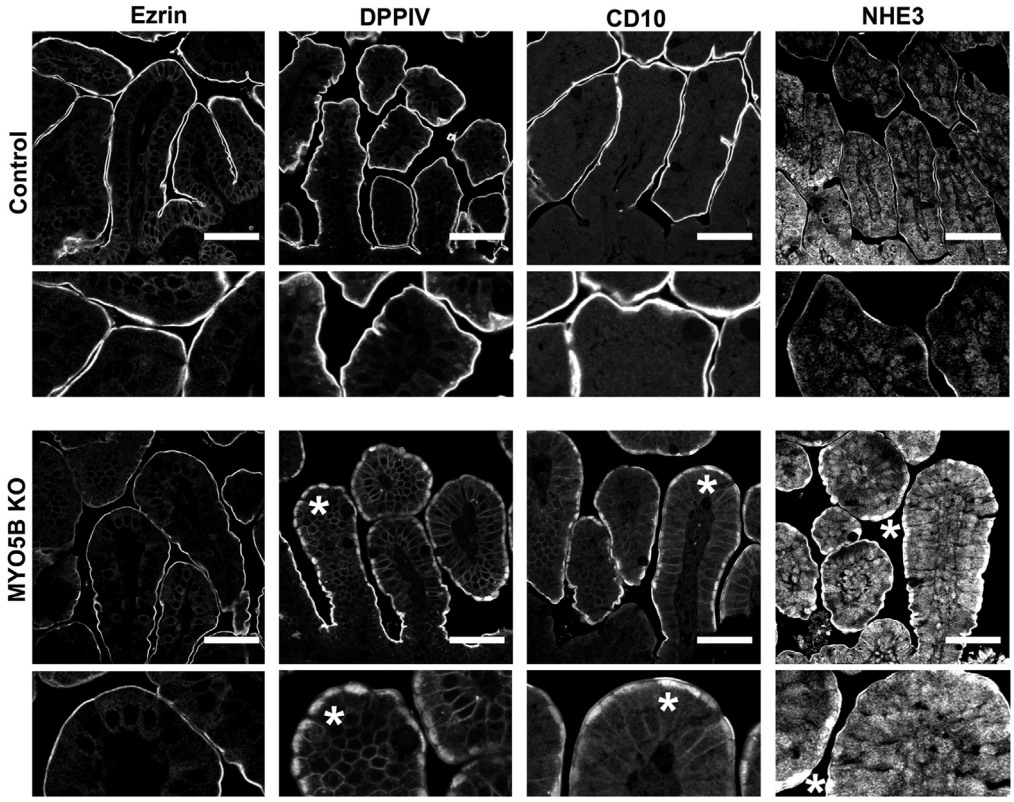

Figure 10. Immunofluorescence staining of embryonic duodenum. Embryonic (E18.5) duodenum from control and MYO5B KO littermates was immunostained for apical markers to examine mistrafficking and microvillus inclusion formation. As in neonates, all markers (ezrin, DPPIV, CD10, and NHE3) labeled the apical membrane in control embryonic duodenum (*top row*). In contrast to neonates, ezrin-positive inclusions were not observed in MYO5B KO duodenum, suggesting that microvillus inclusions were not formed until after birth. However, DPPIV, CD10, and NHE3 staining was collapsed to a subapical localization (*asterisk*) not found in the control littermates. These findings show apical mistrafficking is present before birth, but microvillus inclusions likely do not form until after birth. *Scale bars*: 50 μm.

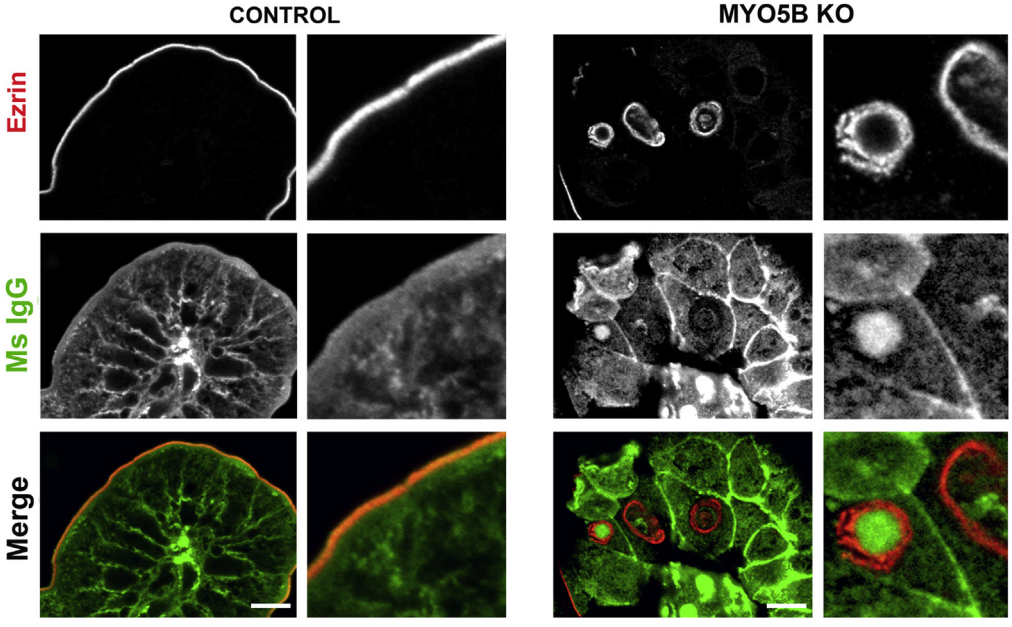

Figure 11. IgG internalization in ezrin-positive inclusions. Mouse IgG internalization was visualized by immunofluorescence staining for mouse IgG (Ms IgG, *green*) and ezrin (*red*). To detect endogenous mouse IgG, the Mouse on Mouse block kit could not be used, thus resulting in high background signal from interstitial cells. Nonetheless, no significant internal mouse IgG was observed in control duodenum (*left panels*). In contrast, in MYO5B KO duodenum, mouse IgG was found inside ezrin-positive inclusions (*right panels*). *Scale bars*: 10 μm.

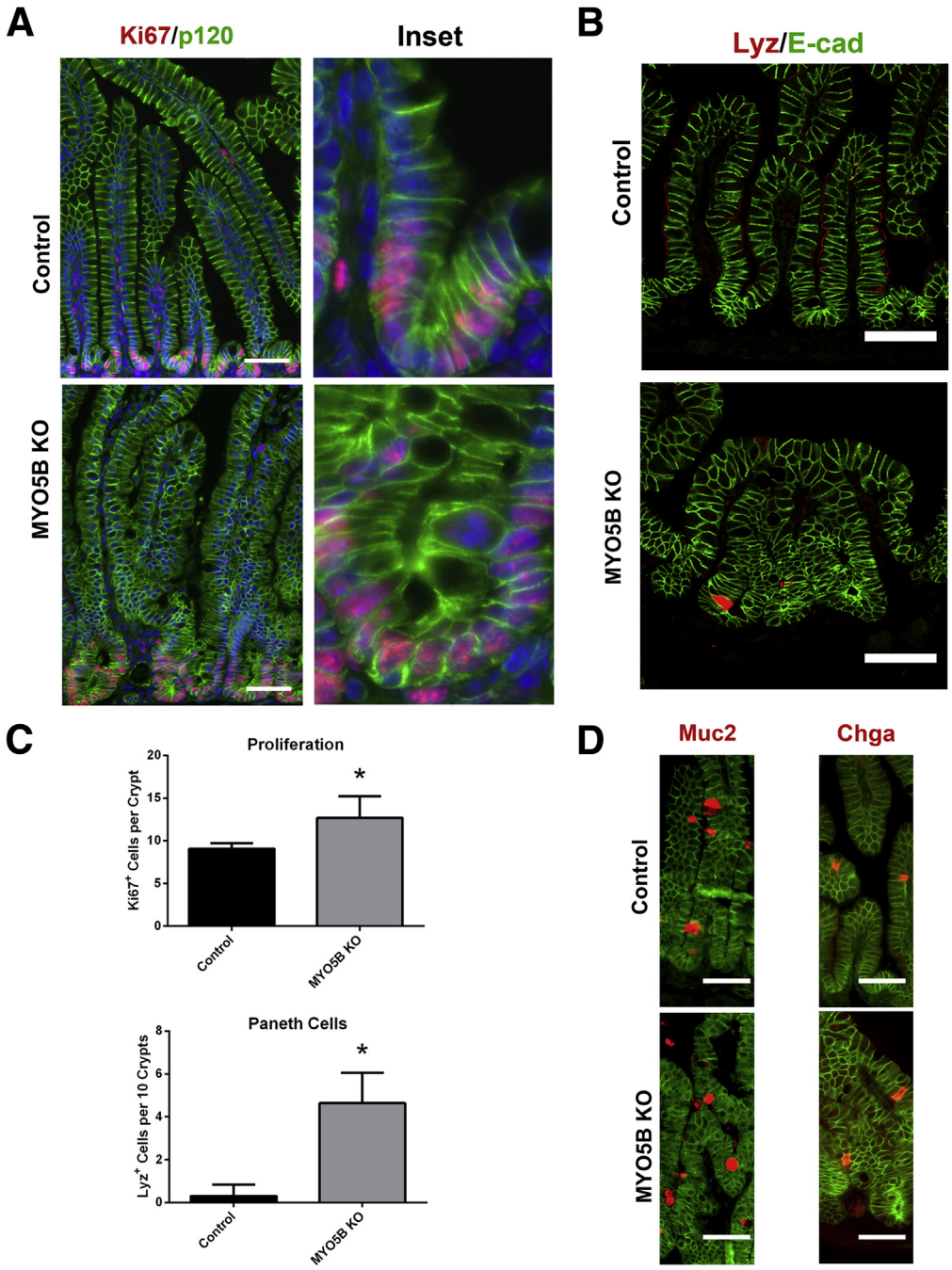

Figure 12. Proliferation and cell lineages in MYO5B KO duodenum. (*A*) Ki67 was used as a marker of proliferation. Sections were stained for Ki67 (red) and p120 (green). Ki67-positive proliferating cells were confined to the short crypts in control mice. In MYO5B KO mice, an increase in proliferation was observed as well as an expansion of the crypt. 4',6-diamidino-2-phenylindole (blue). *Scale bar*: 50 μm. (*B*) To determine the status of Paneth cells, sections were immunostained for Lysozyme (red) and E cadherin (E-cad) (green). A premature maturation of Paneth cells was observed in MYO5B KO duodenum. *Scale bar*: 50 μm. (*C*) The number of Ki67-positive proliferating cells per crypt was quantified for both control and MYO5B KO duodenum. A small but significant increase in proliferation was found in MYO5B KO duodenum. $^*P = .05$. (*B*) Lysozyme-positive Paneth cells appear earlier in MYO5B KO than in control littermates. Although less than 1 Paneth cell per 10 crypts was found in control duodenum, more than 4 Paneth cells per 10 crypts were counted in MYO5B KO duodenum $^*P = .05$. (*D*) Tissue sections were co-stained for lineage markers Muc2 or Chga (red) and p120 (green). Goblet cells (Muc2-positive) and enteroendocrine cells (Chga-positive) were present in both control and MYO5B KO tissue. *Scale bar*: 50 μm.

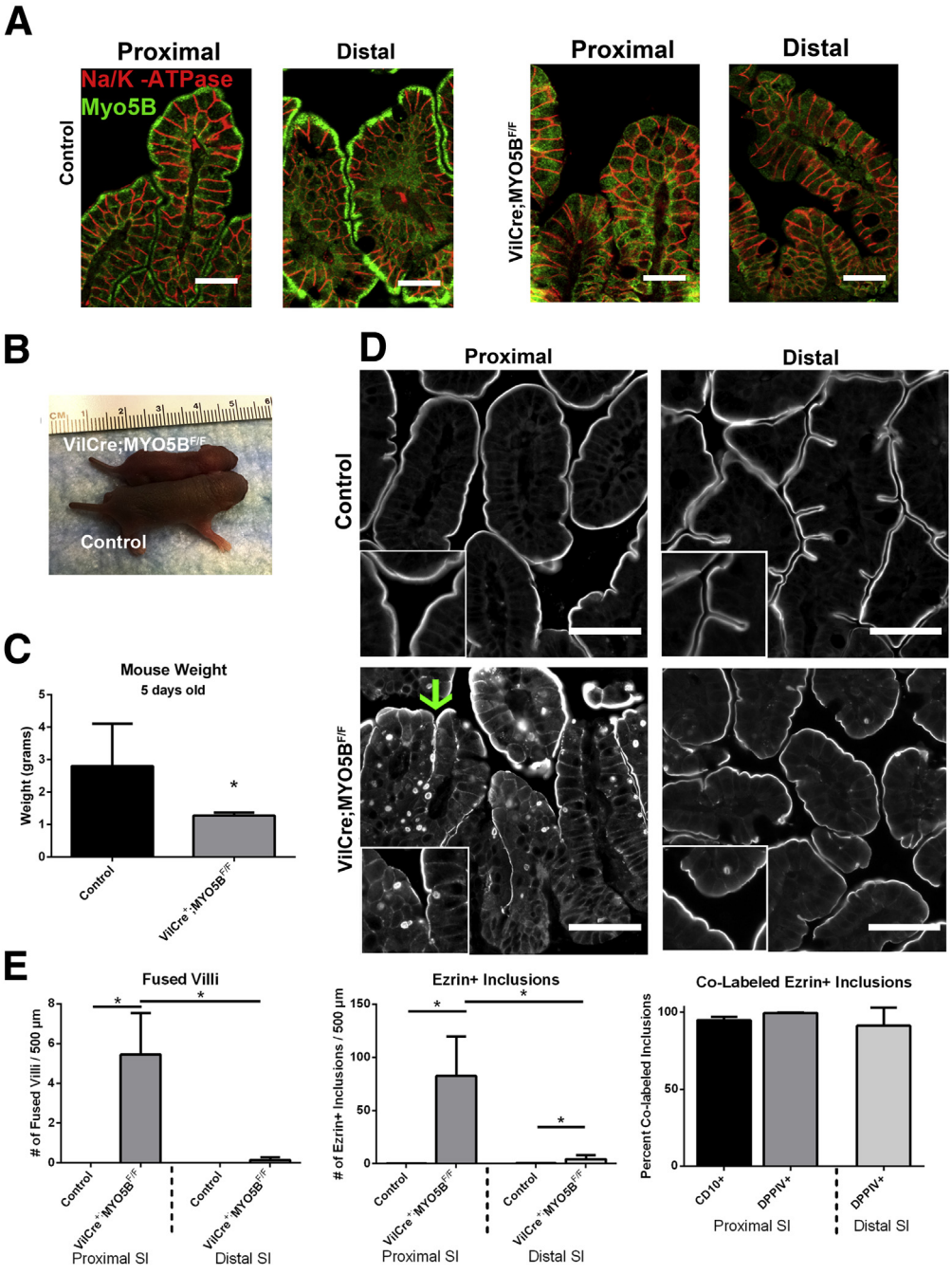

Figure 13. Characterization of VillinCre;MYO5B$^{F/F}$ intestine. (*A*) Proximal and distal small intestine from control and VillinCre;MYO5B$^{F/F}$ mice was immunostained for MYO5B (green) and Na/K-ATPase (red). A clear subapical concentration of MYO5B was observed in control tissue, however, this immunoreactivity was lost in VillinCre;MYO5B$^{F/F}$ intestine (proximal and distal). Of note, no significant changes were observed in Na/K-ATPase expression and localization. *Scale bar*: 25 μm. (*B*) An image of a VillinCre;MYO5B$^{F/F}$ mouse and a control littermate mouse show an obvious size difference. (*C*) Mice weighed at 5 days old showed that VillinCre;MYO5B$^{F/F}$ mice were approximately half the weight of control littermates. *$P = .05$ (*D*) Ezrin immunofluorescence showed fused villi (*green arrow*) and the presence of ezrin-positive inclusions in VillinCre;MYO5B$^{F/F}$ proximal small intestine. However, only occasional inclusions were observed in the VillinCre;MYO5B$^{F/F}$ distal small intestine and, rarely, fused villi (*lower right panel*). *Scale bar*: 50 μm. (*E*) Similar to germline MYO5B KO mice, VillinCre;MYO5B$^{F/F}$ mice showed a gradient of phenotype from proximal to distal small intestine. Approximately 5 fused villi per 500-μm length of proximal intestine was measured, which decreased to only rare fused villi in the distal small intestine. Likewise, the VillinCre;MYO5B$^{F/F}$ small intestine showed significantly fewer inclusions in the distal small intestine compared with proximal. Again, more than 98% of all ezrin-positive inclusions also labeled with CD10 or DPPIV with no significant differences found between the proximal and distal small intestine. *$P = .05$. SI, small intestine.

was lost in VillinCre;MYO5B$^{F/F}$ mouse enterocytes (Figure 14*A*). Localization of these proteins expanded into a more diffuse subapical region as well as localizing to the internal inclusions found in VillinCre;MYO5B$^{F/F}$ mouse duodenum. DPPIV also was dispersed into punctate vesicles within the enterocyte cytoplasm (Figure 14*A*). Examination of DPPIV localization in VillinCre;MYO5B$^{F/F}$ mouse distal small bowel showed near absence of the internal DPPIV-positive punctate vesicles found in the proximal small intestine of VillinCre;MYO5B$^{F/F}$ mice (Figure 14*A*). Although a more diffuse subapical DPPIV localization was noted in the distal small intestine of VillinCre;MYO5B$^{F/F}$ mice than in controls, the clear presence of apical brush-border DPPIV localization, in addition to the lack of DPPIV-positive inclusions and punctate vesicles, further shows the presence of a gradient of pathologic changes upon loss of MYO5B along the small intestine.

To examine the effect of MYO5B loss on apical trafficking and polarity, VillinCre;MYO5B$^{F/F}$ mouse duodenum was immunostained for the apical trafficking proteins Rab8a, Rab11a, and STX3. In control duodenum, Rab8a, Rab11a, and STX3 were concentrated to the subapical region in enterocytes, while Rab8a also was distributed along the lateral membrane (Figure 14*B*). In VillinCre;MYO5B$^{F/F}$ mouse duodenum, Rab8a and Rab11a occasionally localized to inclusions, but overall were dispersed predominately throughout the cytoplasm or lost in enterocytes (Figure 14*B*). Immunostaining for STX3 showed relocation into a more diffuse subapical distribution, as well as localization in the inclusions (Figure 14*B*).

The effects of MYO5B loss on basolateral trafficking were examined by immunostaining for Na/K-ATPase, E-cadherin, and p120. Loss of MYO5B from VillinCre;MYO5B$^{F/F}$ intestine did not significantly affect Na/K-ATPase localization to the basolateral membrane (Figure 13*A*). Similarly, normal localization of E-cadherin and p120 to the lateral membranes was observed in VillinCre;MYO5B$^{F/F}$ mouse duodenum (Figure 14*C*). Although, as previously noted, disruption of villi structure and resulting disorganization of enterocytes may obscure subtle changes in localization of these basolateral proteins, no significant changes were found in the localization of basolateral proteins.

We next examined if internal ezrin-positive inclusions or the internalized DPPIV were co-localized with Lamp2-positive lysosomes. Although some ezrin-positive inclusions did not localize near Lamp2 expression, other ezrin-positive inclusions were surrounded or cupped by Lamp2-positive lysosomes, but did not directly co-localize with Lamp2 (Figure 15*A*). The 2 populations of internalized DPPIV not associated with ezrin-positive inclusions (both diffuse subapical DPPIV and DPPIV in small punctate vesicles) both co-labeled with Lamp2 (Figure 15*A*). These data show that at least a portion of the internalized apical proteins likely are diverted to lysosomes.

The ultrastructure of VillinCre;MYO5B$^{F/F}$ mouse duodenal enterocytes was analyzed by SEM and TEM. Although VillinCre;MYO5B$^{F/F}$ mouse enterocytes maintained apical microvilli, these apical microvilli were significantly shorter and wider than microvilli found in control enterocytes (Figure 16*A*–*C*). In addition, inclusions with mature microvilli frequently were observed in VillinCre;MYO5B$^{F/F}$ enterocytes by TEM (Figure 16*B*). Although apical microvilli in VillinCre;MYO5B$^{F/F}$ enterocytes were significantly shorter, SEM showed that this shortened length did not significantly affect packing or organization (Figure 16*D* and *E*).

VillinCre;MYO5B$^{F/F}$ Mice Do Not Display Changes in Proliferation or Cell Lineage Differentiation

Proliferation in VillinCre;MYO5B$^{F/F}$ duodenal sections was examined by immunostaining for Ki67. As in control duodenum, proliferating cells were confined within crypts (Figure 15*B*). No significant difference was found in the number of proliferating crypt cells between control and VillinCre;MYO5B$^{F/F}$ intestines (Figure 15*B*). In contrast to germline MYO5B KO intestine, only rare lysozyme-positive Paneth cells were observed in VillinCre;MYO5B$^{F/F}$ duodenum (Figure 15*C*). Similarly, no significant differences in the presence of goblet cells or enteroendocrine cells in VillinCre;MYO5B$^{F/F}$ duodenum were observed (Figure 15*C*).

Prominent Mistrafficking and Apical Microvilli Loss, But Not Microvillus Inclusions, Are the Predominate Pathologies of Inducible Intestinal Targeted MYO5B Deletion in Adult Mice

Inducible VillinCre^{ERT2};MYO5B$^{F/F}$ C57BL/6 mice were obtained by crossing MYO5B$^{F/F}$ mice to VillinCre^{ERT2} mice. Induction of MYO5B loss in VillinCre^{ERT2};MYO5B$^{F/F}$ mice was achieved by administration of one intraperitoneal injection of 2 mg of tamoxifen to 8- to 10-week-old mice. Mice showed signs of distress and were killed 3 days after the tamoxifen injection. Tamoxifen-injected MYO5B$^{F/F}$ mice were used as controls. MYO5B loss in both proximal and distal small intestine was confirmed by MYO5B immunostaining (Figure 17*A*). Although no weight differences were observed between VillinCre^{ERT2};MYO5B$^{F/F}$ and control mice, VillinCre^{ERT2};MYO5B$^{F/F}$ mice did develop diarrhea as confirmed by a significantly higher percentage of water present in the stool (Figure 17*B*). Based on our findings from the neonatal loss of MYO5B, we first examined VillinCre^{ERT2};MYO5B$^{F/F}$ mouse small intestines by ezrin immunostaining. In the tamoxifen-induced VillinCre^{ERT2};MYO5B$^{F/F}$ mouse duodenum, ezrin also was found on the apical microvilli, although it appeared as a fainter thinner band along the apical surface or even was completely lost in some cells (Figure 17*C*). Notably, only occasional ezrin-positive inclusions were seen. Indeed, less than one ezrin-positive inclusion was found per 500-μm length of duodenum (and only rarely in the distal small intestine) (Figure 17*D*). In addition, no evidence for fused villi was found in either proximal or distal VillinCre^{ERT2};MYO5B$^{F/F}$ small intestine (Figure 17*D*).

Because ezrin immunostaining suggested a shortened or even lost brush border with only a few intracellular inclusions in VillinCre^{ERT2};MYO5B$^{F/F}$ mouse duodenum, we

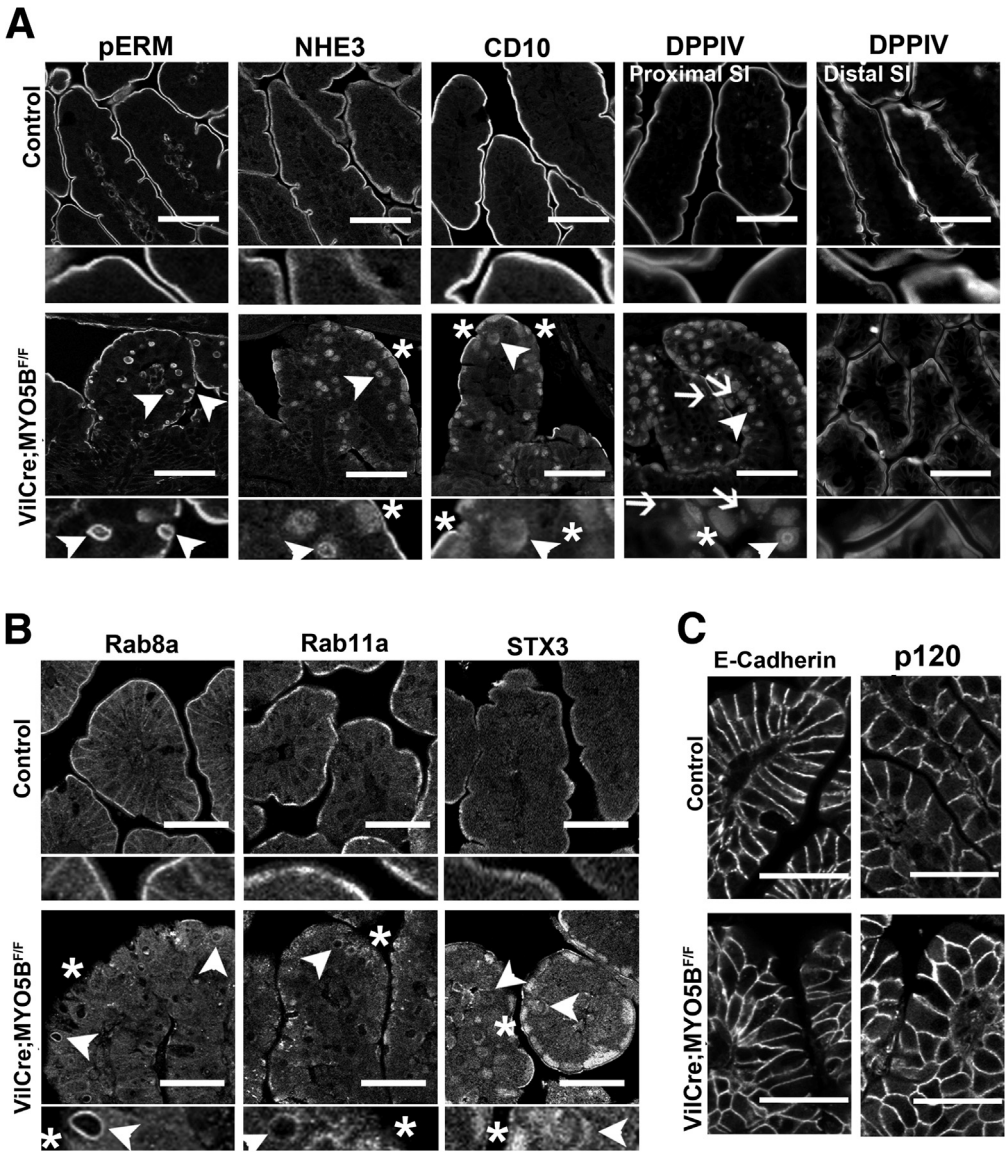

Figure 14. Disruption of apical trafficking in VillinCre;MYO5B$^{F/F}$ duodenum. (*A*) Control (*top row*) and VillinCre;MYO5B$^{F/F}$ (*bottom row*) duodenal sections were immunostained for apical proteins (pERM, NHE3, CD10, and DPPIV). pERM staining in control duodenum showed microvilli located only on the apical surface of the villi enterocytes. In VillinCre;MYO5B$^{F/F}$ duodenum, pERM immunostaining identified microvillus inclusions inside enterocytes as well as the formation of microvillus inclusions at the apical surface of enterocytes (*arrowhead*). The apical exchanger NHE3 normally was located on the apical membrane of enterocytes in the small intestine. Upon MYO5B loss, NHE3 was mislocalized to a diffuse subapical compartment (*asterisk*) and labeled in inclusions (*arrowhead*). CD10 and DPPIV both labeled the apical brush border in control mice. In VillinCre;MYO5B$^{F/F}$ duodenum, CD10 and DPPIV were relocated into a diffuse subapical localization (*asterisk*) as well as into internal inclusions (*arrowheads*). DPPIV also was found localized to small punctate vesicles (*arrows*). In VillinCre;MYO5B$^{F/F}$ distal small intestine (*last column*), although some DPPIV subapical accumulation was observed, no apparent overall difference was noted in comparison with control. *Scale bar*: 50 μm. (*B*) Apical trafficking proteins, Rab8a, Rab11a, and STX3, were concentrated subapically in control tissue, with Rab8a also labeling along lateral membranes. Rab8a and Rab11a were lost from the apical membrane with a small accumulation in the subapical regions (*asterisk*), and occasionally localized to inclusions (*arrowheads*) in VillinCre;MYO5B$^{F/F}$ duodenum. STX3 was collapsed into a diffuse subapical region (*asterisk*) as well as localized to inclusions (*arrowheads*). *Scale bar*: 50 μm. (*C*) Control and VillinCre;MYO5B$^{F/F}$ duodenum were immunostained for E-cadherin and p120. In both controls and VillinCre;MYO5B$^{F/F}$ duodenum, E-cadherin and p120 labeled the basolateral membranes with no obvious differences between them. *Scale bar*: 50 μm. SI, small intestine.

then immunostained for another microvilli brush-border structural protein, villin. In control duodenum, villin lined the wide brush border along the apical surface of enterocytes (Figure 17*C*). Although villin still was localized to the apical surface in VillinCre^{ERT2};MYO5B$^{F/F}$ duodenum, it labeled a thinner band along the enterocyte apical surface and was even absent in some regions (Figure 17*C*). Again, only occasional villin-positive inclusions were found within

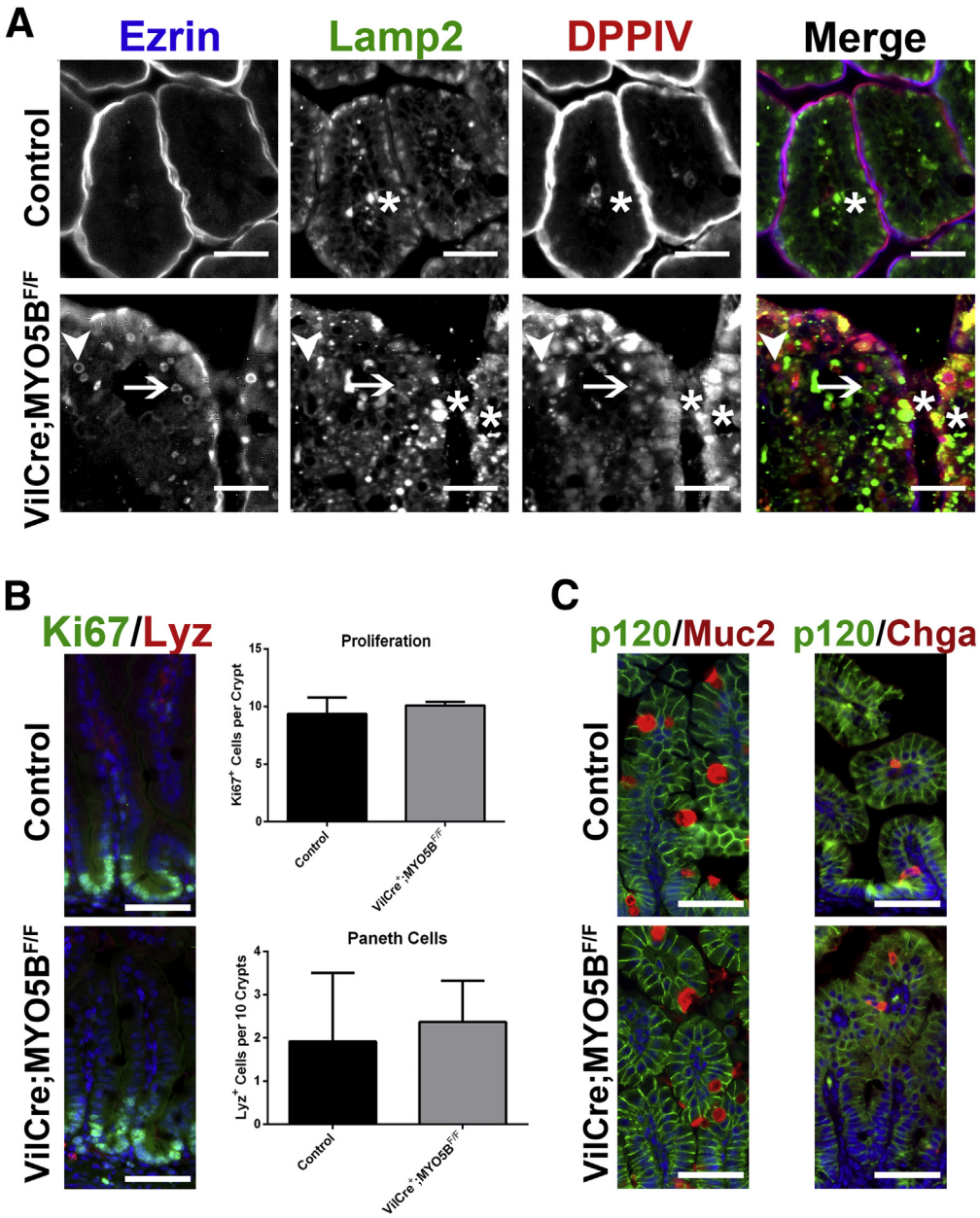

Figure 15. Localization of lysosomes and characterization of cellular make-up in villi. (*A*) Duodenum from control and VillinCre;MYO5B$^{F/F}$ duodenum was triple-stained for ezrin (blue), Lamp2 (green), and DPPIV (red). In control enterocytes, Lamp2-positive lysosomes concentrated just under the ezrin and DPPIV-positive apical surface. In VillinCre;MYO5B$^{F/F}$ duodenum, a subset of ezrin-positive inclusions were surrounded closely or cupped by Lamp2-positive lysosomes (*arrow*). However, other ezrin-positive inclusions were not located near Lamp2 (*arrowhead*). DPPIV internalized into small vesicles co-localized with Lamp2 (*asterisks*). *Scale bar*: 25 μm. (*B*) Control and VillinCre;MYO5B$^{F/F}$ duodenum was analyzed for proliferating cells (Ki67 in green) and the early maturation of Paneth cells (lysozyme in red). No significant differences were found between the 2 mouse strains. 4′,6-diamidino-2-phenylindole (blue). *Scale bar*: 50 μm. (*C*) Sections were immunostained for Muc2 (red, *left panel*) and Chga (red, *right panel*) with p120 (green). Similar to the germline MYO5B KO, no significant difference was observed between the control littermates and VillinCre;MYO5B$^{F/F}$ duodenums. 4′,6-diamidino-2-phenylindole (blue). *Scale bar*: 50 μm.

the enterocytes. These findings suggest that the apical brush border was disrupted upon MYO5B loss in adult mice, but microvillus inclusion formation (as observed by ezrin or villin immunoreactivity) could not account for the diarrhea and dehydration observed in VillinCre^{ERT2};MYO5B$^{F/F}$ mice.

To examine the localization of nonstructural apical components, duodenum sections from tamoxifen-induced adult VillinCre^{ERT2};MYO5B$^{F/F}$ mice were immunostained for CD10 and DPPIV. Loss of MYO5B in VillinCre^{ERT2};MYO5B$^{F/F}$ mouse duodenum resulted in the

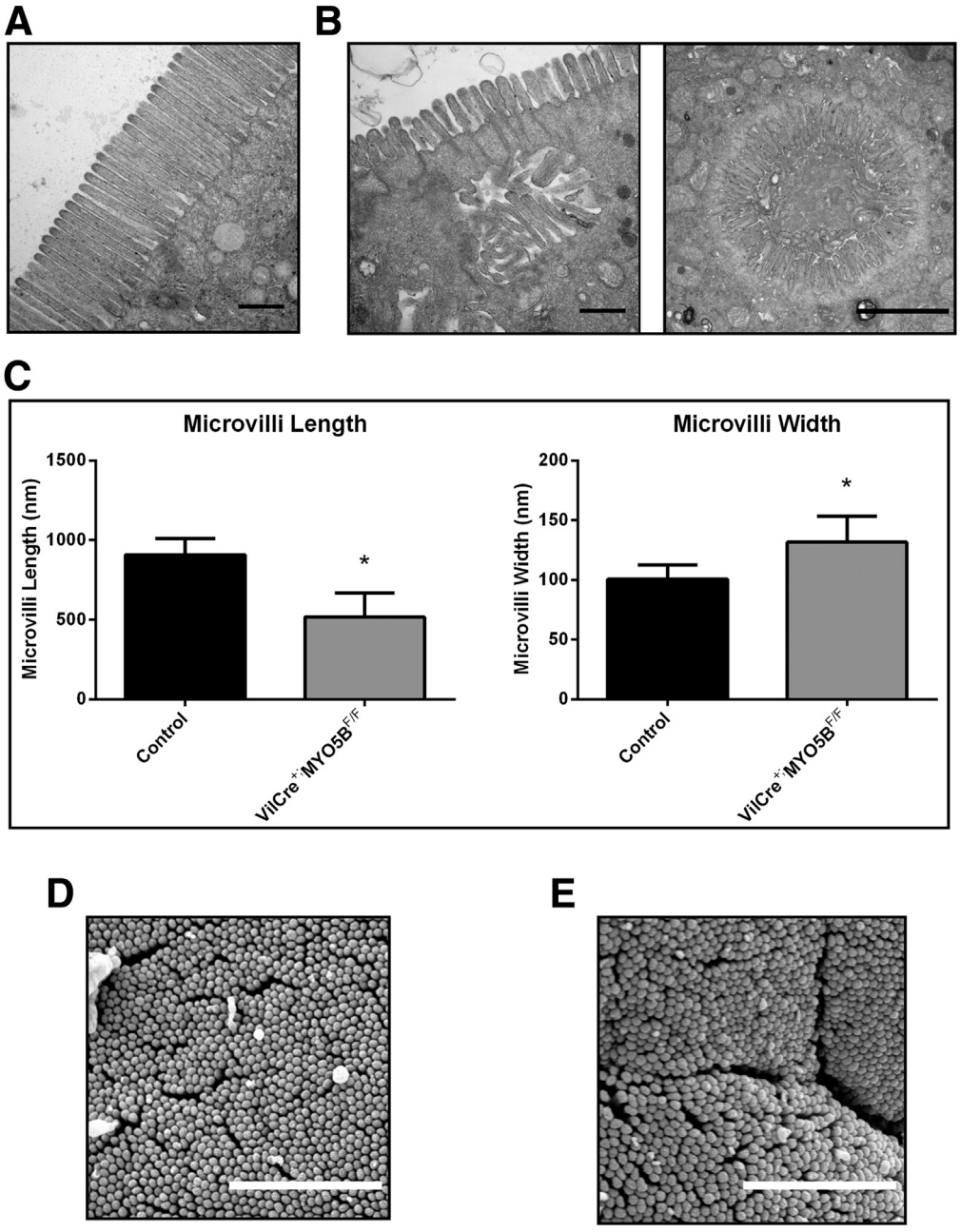

Figure 16. TEM and SEM analysis of apical microvilli in VillinCre;MYO5B$^{F/F}$ mice. (*A*) Control duodenum was imaged by TEM. Images showed long and straight microvilli on the apical surface of enterocytes. *Scale bar*: 500 nm. (*B*) TEM imaging of VillinCre;MYO5B$^{F/F}$ duodenum showed shortened apical microvilli and the presence of internal inclusions with obvious microvilli. *Scale bar*: 500 nm (*left panel*). TEM analysis also showed internal microvillus inclusions with fully formed microvilli. *Scale bar*: 2 μm (*right panel*). (*C*) The length and width of apical microvilli from control and VillinCre;MYO5B$^{F/F}$ duodenum was measured. In VillinCre;MYO5B$^{F/F}$ duodenum, microvilli were significantly shorter than control microvilli. In addition, microvilli also were wider in VillinCre;MYO5B$^{F/F}$ duodenal enterocytes. *$P < .05$. (*D*) Control duodenum examined by SEM showed tightly packed microvilli. *Scale bar*: 2 μm. (*E*) By SEM, tightly packed microvilli were visualized in VillinCre;MYO5B$^{F/F}$ duodenum, showing that packing remained largely unchanged even with shortened microvilli. *Scale bar*: 2 μm.

mislocalization of both CD10 and DPPIV. CD10 was collapsed into a broad and diffuse subapical localization as well as diverted to vesicular structures (Figure 18*A*). DPPIV also was mislocalized to a subapical region, in addition to localization in punctate vesicles inside enterocytes (Figure 18*B*). As in neonates, Lamp2-positive lysosomes were concentrated to a narrow subapical region just under the CD10- and DPPIV-labeled brush border in control adult duodenum. However, in VillinCre^{ERT2};MYO5B$^{F/F}$ mouse duodenum, a subset of internalized CD10 co-localized with Lamp2 (Figure 18*A*). Similarly, a portion of internalized DPPIV also co-localized with Lamp2 (Figure 18*B*). Thus, upon MYO5B loss, in the duodenum internalized apical proteins, CD10 and DPPIV, were relocalized to Lamp2-positive lysosomes. Nevertheless, little internalized DPPIV was observed in the enterocytes of the distal small intestine (Figure 18*B*).

Because apical proteins were mislocalized in tamoxifen-induced VillinCre^{ERT2};MYO5B$^{F/F}$ mouse duodenum, disruption of apical trafficking and polarity was investigated. In VillinCre^{ERT2};MYO5B$^{F/F}$ mouse duodenum, NHE3 was mislocalized to a diffuse and broad subapical compartment (Figure 19*A*). To further investigate apical trafficking, Rab8a and Rab11a expression and distribution were assessed. The predominant subapical concentration of Rab8a was lost in VillinCre^{ERT2};MYO5B$^{F/F}$ enterocytes. Instead, Rab8a was

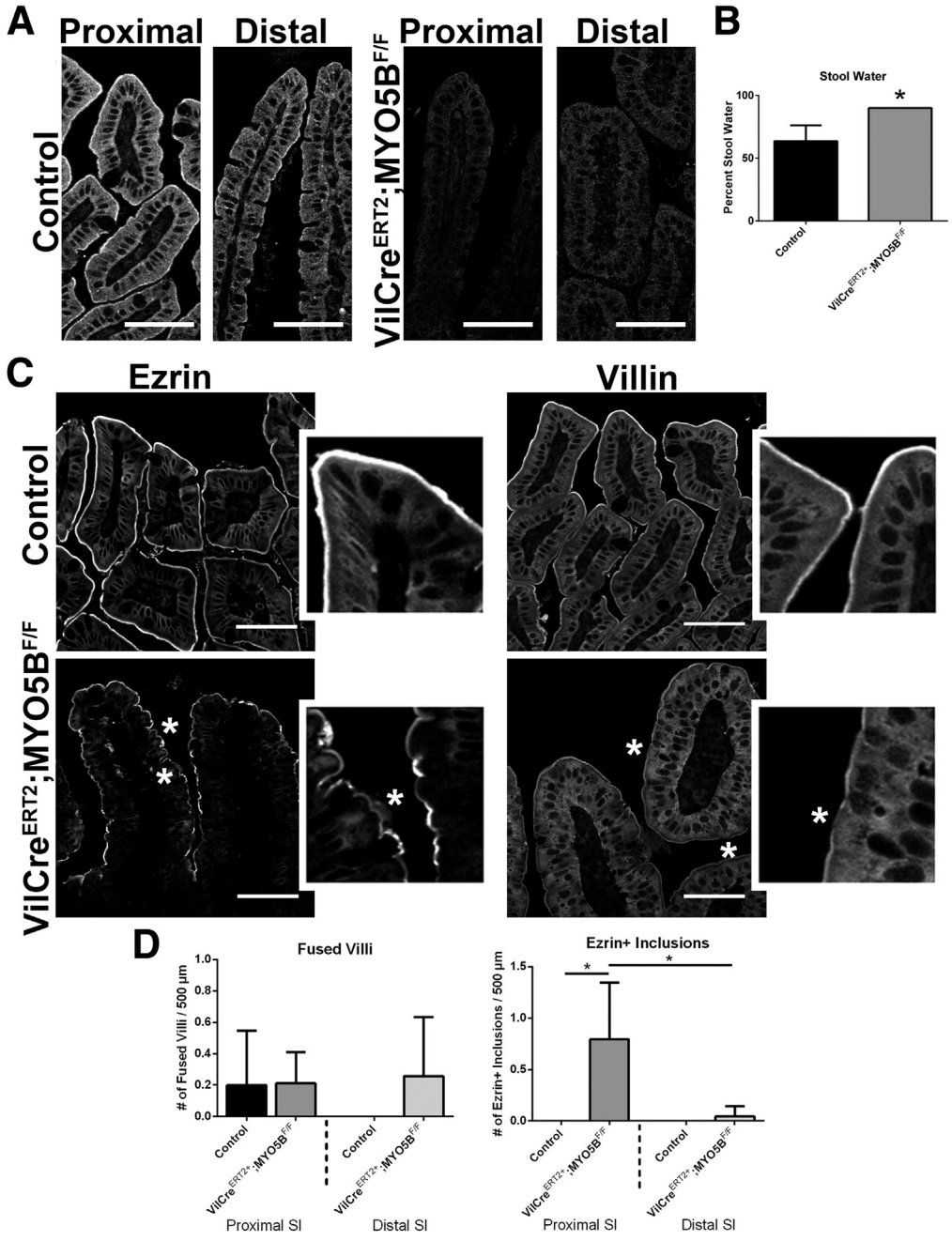

Figure 17. Characterization of VillinCre^{ERT2};MYO5B$^{F/F}$ mouse small intestine in 8-week-old mice induced with tamoxifen. Eight-week-old VillinCre^{ERT2};MYO5B$^{F/F}$ mice were treated with a single 2 mg intraperitoneal dose of tamoxifen to induce intestine KO of MYO5B. (*A*) Proximal and distal small intestine from control and VillinCre^{ERT2};MYO5B$^{F/F}$ mice were immunostained for MYO5B. A clear subapical concentration of MYO5B was observed in control tissue, however, MYO5B immunofluorescence was lost in VillinCre^{ERT2};MYO5B$^{F/F}$ mice in both proximal and distal intestine. *Scale bar*: 50 μm. (*B*) The percentage of stool constituted by water was determined in control and VillinCre^{ERT2};MYO5B$^{F/F}$ mice. VillinCre^{ERT2};MYO5B$^{F/F}$ mice had significantly higher water content in stool collected from the colon (90% stool water). *$P = .05$. (*C*) Ezrin immunostaining in control mice showed a fully formed brush border along the length of the villi. *Inset*: a strong sharp band of ezrin-positive brush border. In VillinCre^{ERT2};MYO5B$^{F/F}$ duodenum, ezrin labeled a thin band along the brush border, suggesting a shortening or loss of apical microvilli (*asterisk*). Of note, only occasional ezrin-positive inclusions were observed in VillinCre^{ERT2};MYO5B$^{F/F}$ mouse intestines. Similarly, villin labeled a bright and wide brush border in control duodenums. In VillinCre^{ERT2};MYO5B$^{F/F}$ duodenums, the apical villin stain was much thinner and even absent in some locations (*asterisk*), with only rare inclusions observed. *Scale bar*: 50 μm. (*D*) Fused villi and the total number of ezrin-positive inclusions were quantified. No difference was observed in the number of fused villi in control and VillinCre^{ERT2};MYO5B$^{F/F}$ proximal and distal small intestine. There was a significant increase in the number of ezrin-positive inclusions as compared with control in the proximal intestine. However, the total number of inclusions was only 0.75 ezrin-positive inclusions per 500 μm of tissue in VillinCre^{ERT2};MYO5B$^{F/F}$ duodenums. *$P = .05$. SI, small intestine.

more dispersed in a cytoplasmic vesicular distribution, although some Rab8a still was found subapically and along the lateral membrane (Figure 19*A*). Similarly, Rab11a also was redistributed from the subapical region to diffuse cytoplasmic vesicles (Figure 19*A*).

Although our studies here have shown that MYO5B loss in neonates did not cause significant changes in basolateral protein localization, previous studies have reported disruption of basolateral trafficking upon MYO5B loss.[2,3,8,9,11] Again, Na/K-ATPase, E-cadherin, and p120 immunostaining was assessed as an indicator of disruption of basolateral trafficking. In VillinCre^{ERT2};MYO5B$^{F/F}$ mouse enterocytes, Na/K-ATPase still was localized to the basolateral membrane, however, it also was observed in cytoplasmic vesicles in some cells (Figure 19*B*). Similarly, E-cadherin also was mislocalized to cytoplasmic vesicles in addition to the normal basolateral localization (Figure 19*B*). The most prominent effect of MYO5B loss on basolateral proteins was the mislocalization of p120. Loss of MYO5B in adult duodenum resulted in p120 mislocalization to cytoplasmic vesicles similar to that found with Na/K-ATPase and E-cadherin (Figure 19*B*). In addition, p120 also was dispersed into a diffuse cytoplasmic distribution in some enterocytes (Figure 19*B*). These findings suggest that MYO5B loss in adult duodenum can disrupt basolateral trafficking dynamics.

Based on our evidence of diminished ezrin and villin immunostaining of the brush border in adult VillinCre^{ERT2};MYO5B$^{F/F}$ mouse enterocytes, we performed TEM and SEM analysis to assess the status of apical microvilli. By TEM analysis, we observed a heterogeneous pattern for microvilli upon MYO5B loss in adult duodenal enterocytes. Some areas of enterocytes had shorter and wider microvilli in tamoxifen-induced VillinCre^{ERT2};MYO5B$^{F/F}$ enterocytes (Figure 20*A*–*C*), similar to the pattern found in the neonatal MYO5B loss models. In contrast to the neonates, some regions of enterocytes showed only few and sparse microvilli or even complete loss of microvilli (Figure 20*B*). In areas of short microvilli, the microvilli remained normally packed as assessed by SEM (Figure 20*E*). Cross-sections of other regions showed malformed microvilli that appeared to be pinched into segments (Figure 20*E*). This analysis of ultrastructure confirmed that MYO5B loss in adult enterocytes resulted in aberrant microvilli structure or even microvilli loss in some enterocytes. This disturbance of the brush border, in addition to the apical and basolateral mistrafficking, may contribute to the resulting diarrhea seen after induction of MYO5B loss in adult VillinCre^{ERT2};MYO5B$^{F/F}$ mice.

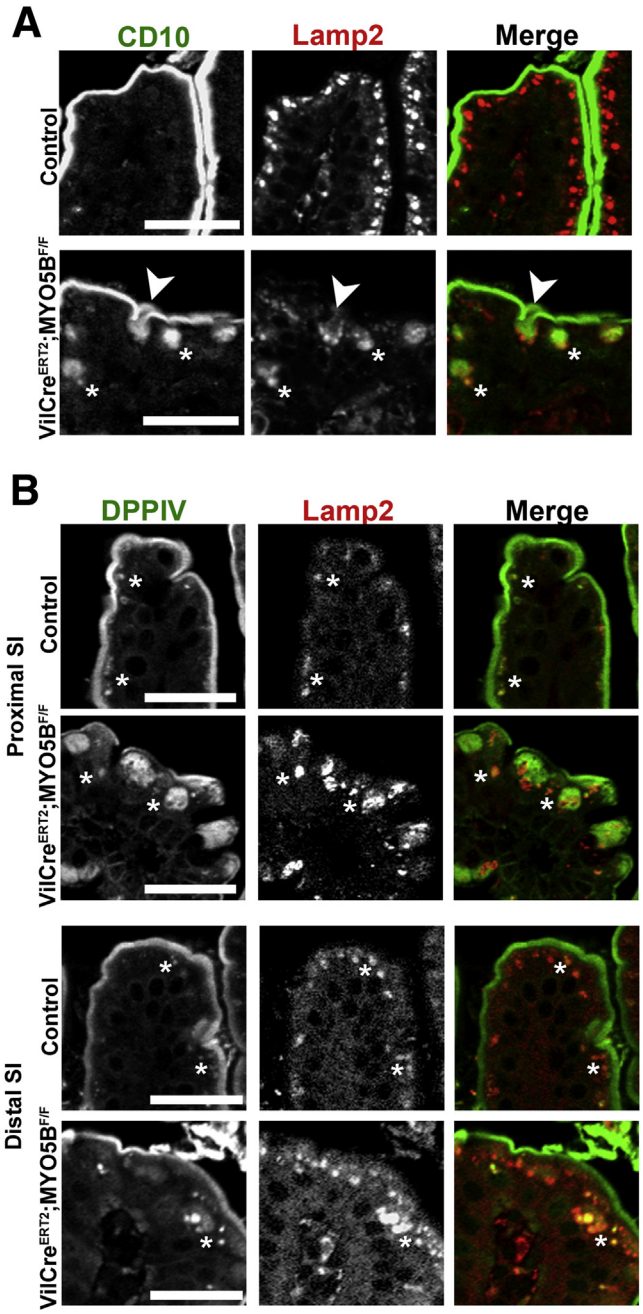

Figure 18. Internalization and trafficking of CD10 and DPPIV to lysosomes. (*A*) Duodenum from control and VillinCre^{ERT2};MYO5B$^{F/F}$ mice were co-stained for CD10 (green) and Lamp2 (red). In control enterocytes, Lamp2-positive lysosomes were located just under the CD10-labeled apical surface. Upon induced MYO5B loss, a subset of CD10 was internalized (*asterisks* and *arrow*). Lamp2 was found surrounding CD10 as it was internalized from the apical surface (*arrow*), and, in addition, Lamp2 co-localized with internal CD10 populations (*asterisks*). *Scale bar*: 25 μm. (*B*) Proximal and distal small intestine from controls and VillinCre^{ERT2};MYO5B$^{F/F}$ mice were immunolabeled for DPPIV (green) and Lamp2 (red). In both proximal and distal small intestine controls, DPPIV predominately resided at the brush border, but a small DPPIV population was found in the subapical region co-localized with Lamp2 (*asterisks*). In VillinCre^{ERT2};MYO5B$^{F/F}$ duodenum, DPPIV was collapsed into a diffuse subapical region as well as to small punctate vesicles (*asterisks*). The DPPIV-labeled vesicles, along with a portion of the diffuse DPPIV staining, co-labeled with Lamp2 (*asterisks*). In VillinCre^{ERT2};MYO5B$^{F/F}$ distal small intestine, most DPPIV was retained on the apical membrane with a small subset of internalized DPPIV found in the small vesicles (*asterisk*). As in the duodenum, this internalized DPPIV population co-labeled with Lamp2 (*asterisk*). *Scale bar*: 25 μm. SI, small intestine.

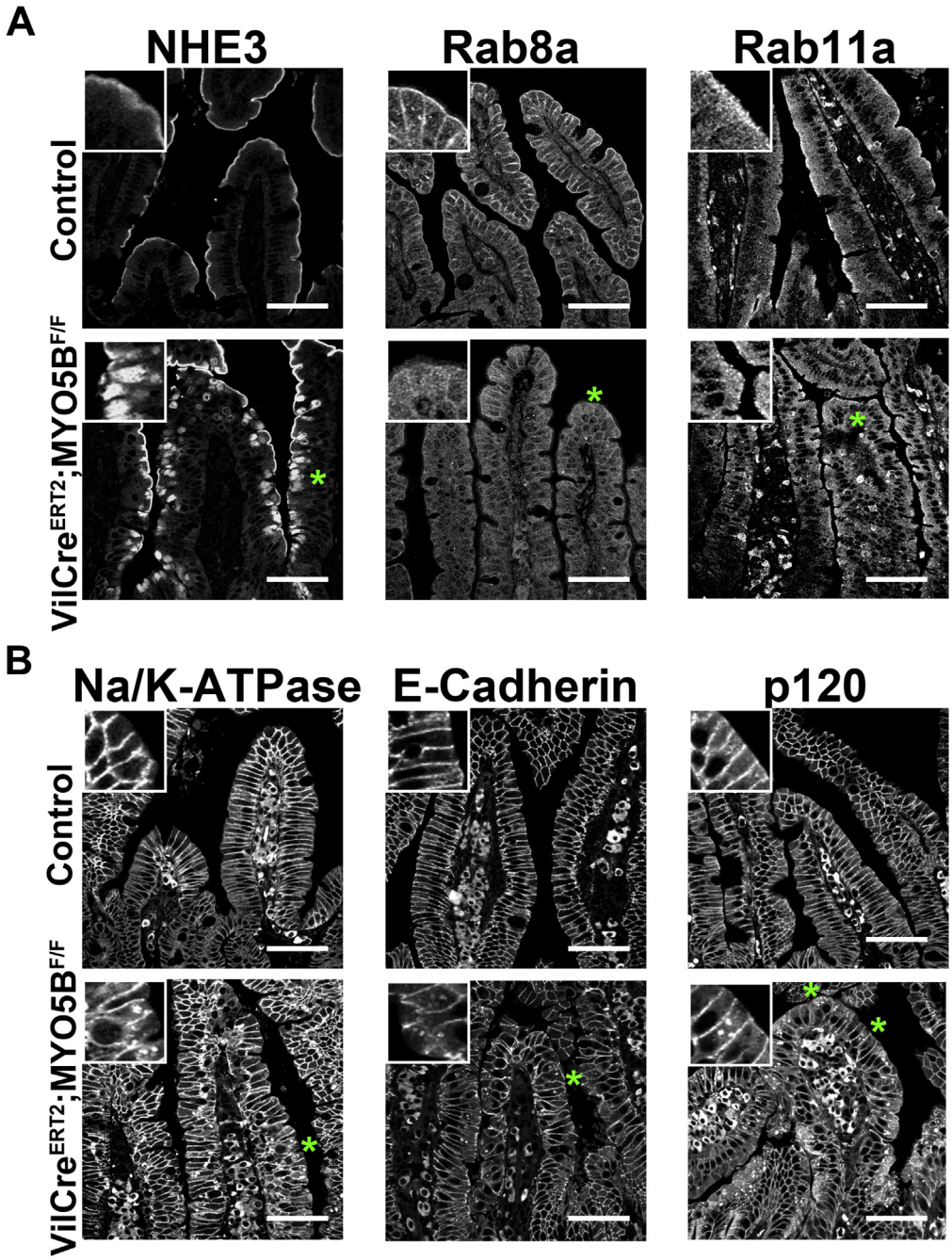

Figure 19. Disruption of apical and basolateral trafficking in VillinCre^{ERT2};MYO5B$^{F/F}$ mice. (*A*) Control and VillinCre^{ERT2};MYO5B$^{F/F}$ duodenum was stained for an apical exchanger protein (NHE3) and for apical trafficking proteins (Rab8a and Rab11a). The normal apical localization of NHE3 (*top left panel*) found in control duodenum was collapsed to a diffuse pattern in the cytoplasm in VillinCre^{ERT2};MYO5B$^{F/F}$ duodenum (*green asterisk*). Correspondingly, the normal concentrated subapical localization of Rab8a and Rab11a was disrupted in VillinCre^{ERT2};MYO5B$^{F/F}$ duodenum (*green asterisks*). In VillinCre^{ERT2};MYO5B$^{F/F}$ duodenum, Rab8a and Rab11a was prominently lost from the subapical region and diverted to a very diffuse cytoplasmic localization. *Scale bar*: 50 μm. (*B*) Basolateral trafficking was analyzed by immunostains for Na/K-ATPase, E-cadherin, and p120 in control and VillinCre^{ERT2};MYO5B$^{F/F}$ duodenum. In control duodenum, all 3 proteins were tightly localized to the basolateral membrane of enterocytes. Although some normal basolateral localization was retained in VillinCre^{ERT2};MYO5B$^{F/F}$ duodenum, aberrant small internal punctate vesicles also were observed for Na/K-ATPase, E-cadherin, and p120 (*green asterisks* and *insets*), suggesting that loss of MYO5B disrupts basolateral trafficking. *Scale bar*: 50 μm.

VillinCre^{ERT2};MYO5B$^{F/F}$ Mice Show Crypt Hyperproliferation

VillinCre^{ERT2};MYO5B$^{F/F}$ duodenum sections were immunostained for Ki67 to examine the effect of MYO5B loss on crypt cells. A significant increase in proliferating cells within VillinCre^{ERT2};MYO5B$^{F/F}$ crypts was observed as compared with control crypts (22 cells per crypt to 15 cells per crypt, respectively) (Figure 20*F* and *G*). These findings resembled the hyperproliferation observed in germline MYO5B KO mice. No proliferating cells were observed outside of crypts in VillinCre^{ERT2};MYO5B$^{F/F}$ duodenum.

Induced MYO5B Loss in VillinCre^{ERT2};MYO5B$^{F/F}$ Neonates Causes Microvillus Inclusion Formation

Together, our studies of both neonate and adult MYO5B loss suggest that the neonatal duodenum is primed for microvillus inclusion formation, consistent with the relative absence of inclusions after induction of MYO5B loss in adults. To test this hypothesis, we induced MYO5B loss in 2-day-old VillinCre^{ERT2};MYO5B$^{F/F}$ and killed the neonates 3 days later (the same timeline used in adult VillinCre^{ERT2};MYO5B$^{F/F}$ mouse studies). MYO5B loss was achieved in the bottom portion of most villi (Figure 21). As seen in the other neonatal MYO5B loss models as well as in

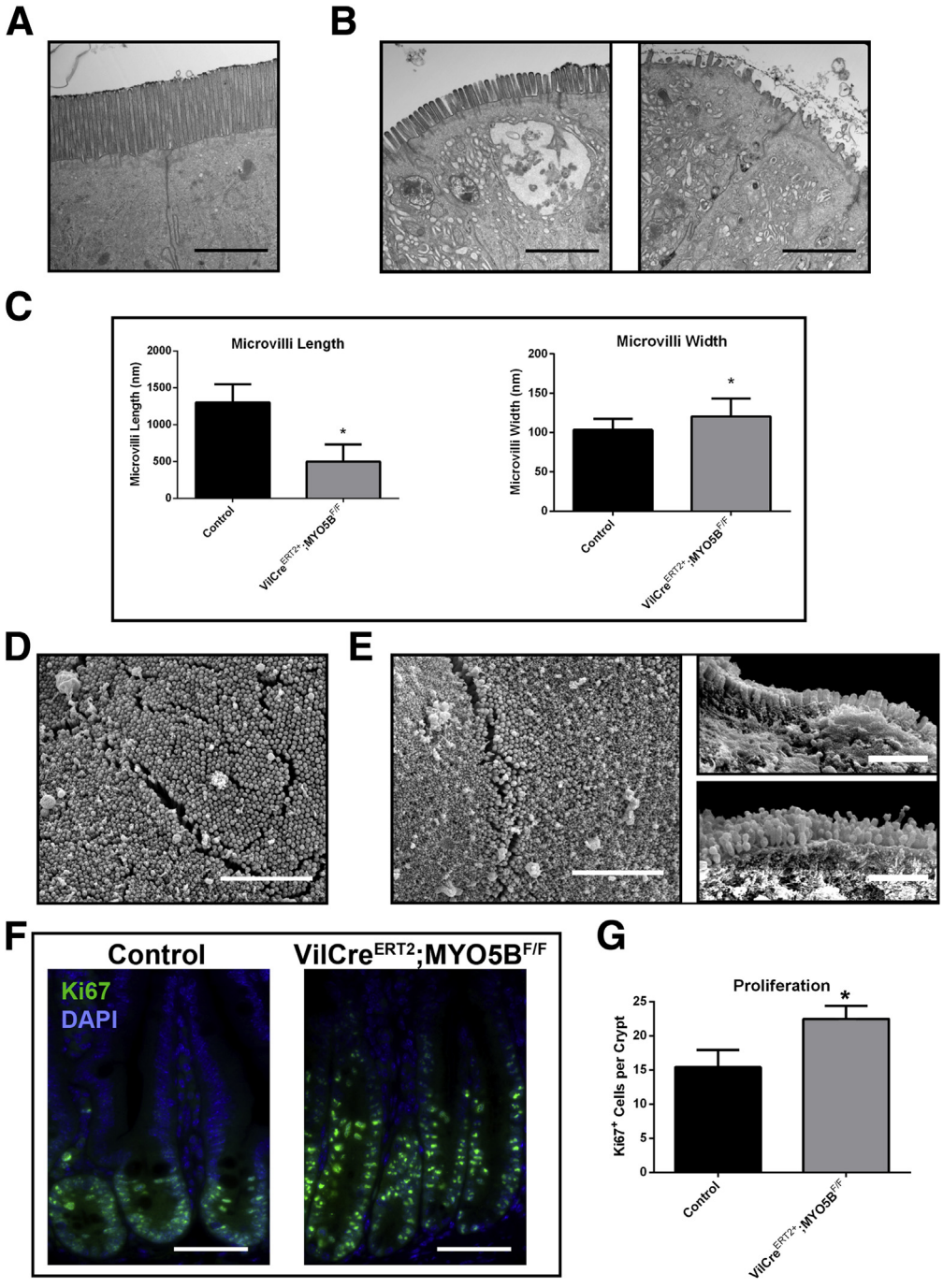

VillinCre^{ERT2};MYO5B$^{F/F}$ adult mice, DPPIV was mislocalized to a diffuse subapical region upon MYO5B loss (Figure 21). Ezrin immunostaining also showed the development of numerous ezrin-positive inclusions in the same enterocytes with DPPIV mislocalization. The number of ezrin-positive inclusions more closely resembled the results found in the germline or constitutive VillinCre-directed neonatal MYO5B KO mice.

Discussion

The present results suggest that the microvillus inclusions associated with loss of functional MYO5B are not central to the pathologic symptoms of microvillus inclusion disease. Thus, induction of MYO5B loss in adult mice led to rapid development of diarrhea, but did not induce the formation of significant numbers of microvillus inclusions. Nevertheless, germline and constitutive targeted knockout of MYO5B did show clear microvillus inclusion formation in the duodenum. In addition, in conditional KO mice induced at 2 days of age, we also observed formation of a prominent number of inclusions in the duodenum. It therefore appears likely that the deletion of MYO5B in the neonatal period has exposed a critical apical membrane internalization paradigm that is specifically active in the neonatal period. The most likely pathway shown would be an apical macropinocytotic route, as we previously showed in CaCo2–BBE cells.[9] Internalization and transcytosis of maternal IgGs in the neonatal period is a critical process for immune protection of newborns.[23] Previous investigations in rats have noted that this pathway is substantially down-regulated after weaning.[24] The relative absence of microvillus inclusions in conditional allele mice induced at 8 weeks of age suggests that this apical macropinocytotic pathway is abolished after the neonatal period. Importantly, we have shown here that microvillus inclusions in MYO5B germline knockout mice contained IgG. During the neonatal period, this apical macropinocytotic route may complement the previously described internalization pathways that may provide for ongoing IgG internalization in the distal intestine and after weaning.[25] These findings support the origin of microvillus inclusions as macropinocytotic events and electron micrographs show the formation of the inclusions from invaginations of the apical membrane. Our previous studies in CaCo2–BBE cell MYO5B knockdown and restitution studies have shown the origin of microvillus inclusions from internalization of the apical membrane.[9] Interestingly, previous studies have shown that FcRN internalization of IgG in CaCo2 cells occurs through an apical internalization pathway most consistent with macropinocytosis.[26] All of these results suggest that the presence of microvillus inclusions reflects internalization of apical membranes in neonatal duodenal enterocytes. The manifestation of the inclusions therefore would represent a failure of enterocytes to recycle these membranes through a MYO5B and Rab11a-dependent process, as previously observed in CaCo2 cells.[9] Indeed, while this manuscript was under review, Vogel et al[27] provided further detail of the deficits in Rab11a- and Rab8a-mediated apical recycling in CaCo2 cells with gene editing–mediated loss of MYO5B.

Although microvillus inclusions may not account for the pathology of diarrheal disease, it appears more likely that symptoms accrue from deficits in apical delivery or maintenance of critical transporters and enzymes in the microvillar brush border. As we have described previously in both Navajo MVID patients and MYO5B CaCo2–BBE knockdown lines,[9] DPPIV was observed prominently in Lamp2-positive lysosomes in the MYO5B knockout mouse models. This phenotype was present in both germline mice and in adult mice with induced intestinal knockout. Also as in previous studies,[11,17] we found dispersal of the normal subapical localization of both Rab8a and Rab11a. These results appear compatible with a failure to execute appropriate recycling of apical membrane constituents and their eventual shunting to the lysosomes for degradation. An absence of apical transporters such as NHE3 or sodium glucose cotransporter 1 could account for the severe diarrhea.

While this manuscript was in preparation, 2 other groups reported mouse models for MYO5B deletion. Carton-Garcia et al[10] reported a germline gene-trap knockout mouse for MYO5B. These mice died during their first day of life. As seen in our studies, they developed microvillus inclusions in the duodenum. This early death for the mice made further detailed analysis difficult. We were unable to produce viable germline offspring on a pure C57BL/6 background, and this seems to correlate with the findings in

Figure 20. (***See previous page***). **Proliferation and EM analysis of VillinCre^{ERT2};MYO5B$^{F/F}$ duodenum.** (*A*) TEM images of control duodenum showed long and straight microvilli on the apical surface of enterocytes. *Scale bar*: 2 μm. (*B*) By TEM analysis, VillinCre^{ERT2};MYO5B$^{F/F}$ duodenum showed varying aberrations in the apical microvilli. Frequent areas of shortened apical microvilli (*left panel*) were observed as well as patches of apical microvilli denudation (*right panel*). *Scale bar*: 2 μm. (*C*) The length and width of apical microvilli from control and VillinCre^{ERT2};MYO5B$^{F/F}$ duodenal enterocytes was quantified. In VillinCre^{ERT2};MYO5B$^{F/F}$ duodenal enterocytes, microvilli that were observed were significantly shorter than control microvilli. In addition, apical microvilli were also wider in VillinCre^{ERT2};MYO5B$^{F/F}$ duodenal enterocytes. *$P < .05$. (*D*) Control duodenum examined by SEM showed tightly packed microvilli. *Scale bar*: 2 μm. (*E*) By SEM, areas of tightly packed microvilli were visualized in VillinCre^{ERT2};MYO5B$^{F/F}$ duodenum, as were areas of shortened microvilli. *Scale bar*: 2 μm (*left panel*). In addition, SEM analysis of some cross-sectioned enterocytes further confirmed areas of short microvilli (*top right panel*; *scale bar*: 1 μm) as well as showed aberrant microvilli morphology such as a linked appearance (*bottom right panel*; *scale bar*: 1 μm). (*F*) Proliferation in control and VillinCre^{ERT2};MYO5B$^{F/F}$ duodenum was examined via Ki67 (green) and 4′,6-diamidino-2-phenylindole (DAPI) (blue) immunofluorescence. Proliferation (noted by Ki67 immunoreactivity) was restricted to the crypts in both control and VillinCre^{ERT2};MYO5B$^{F/F}$ duodenum. *Scale bar*: 50 μm. (*G*) The number of Ki67-positive cells per crypt was quantified for comparison. A significant increase in proliferation was seen in VillinCre^{ERT2};MYO5B$^{F/F}$ duodenal crypts compared with control duodenal crypts. *$P = .05$.

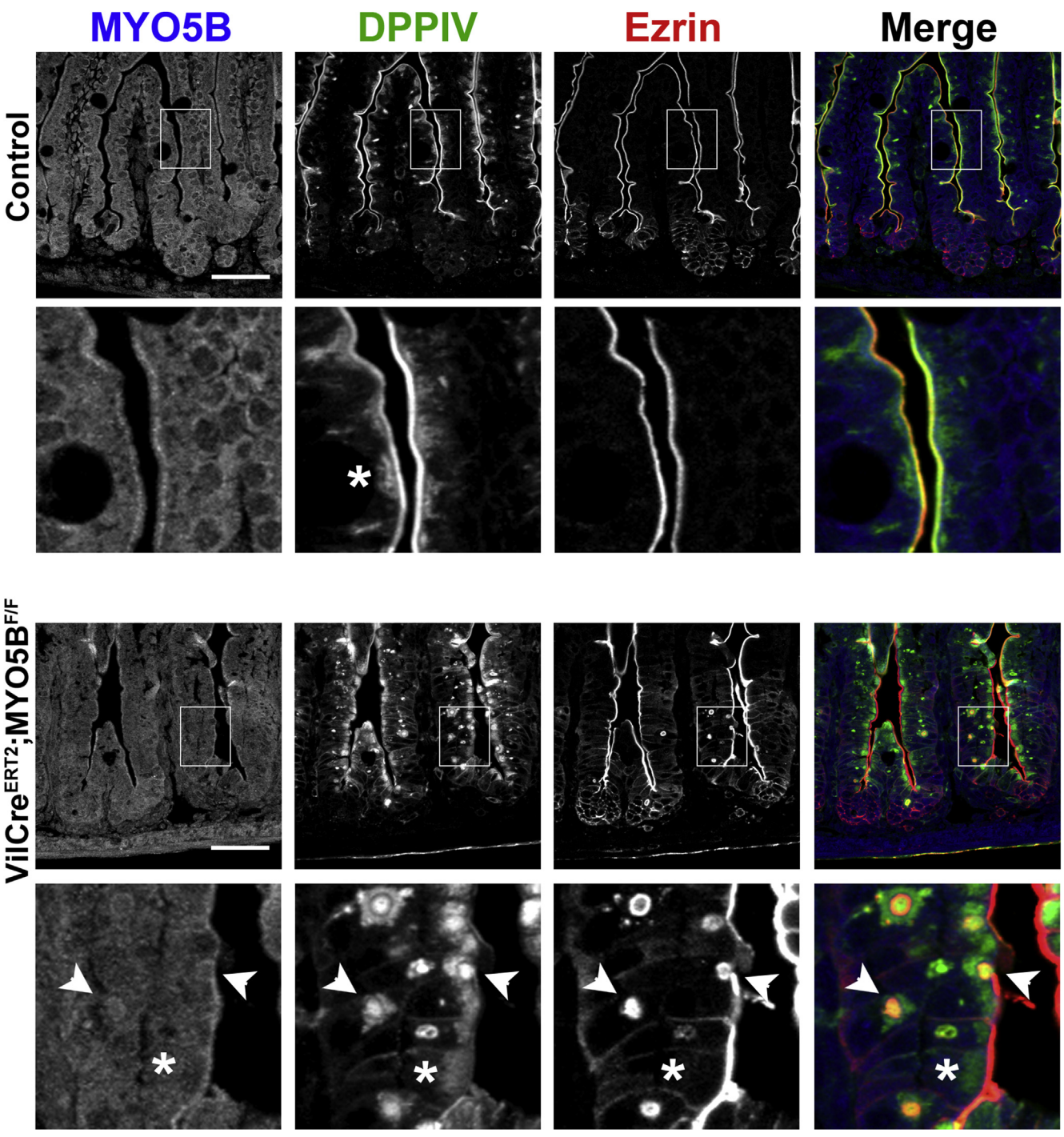

Figure 21. Neonatal induction of MYO5B loss in VillinCre^{ERT2};MYO5B$^{F/F}$ mice. Tamoxifen-induced MYO5B loss in 2-day-old littermates of controls (*top row* and *second inset row*) and VillinCre^{ERT2};MYO5B$^{F/F}$ mice (*third row* and *bottom inset row*) was examined to analyze the formation of microvillus inclusions in neonates as compared with adult VillinCre^{ERT2};MYO5B$^{F/F}$ mice. Sections of duodenum were triple-stained for MYO5B (blue), DPPIV (green), and ezrin (red). In controls, MYO5B localized to the subapical region just below the DPPIV and ezrin-positive co-labeled brush border. Some diffuse internal DPPIV is observed in controls (*asterisk*). In VillinCre^{ERT2};MYO5B$^{F/F}$ neonatal duodenum, the prominent MYO5B subapical localization was lost in the bottom portion of villi. Of note, MYO5B was not completely lost from the upper half of villi. DPPIV was lost from the apical membrane and collapsed into a prominent, diffuse subapical region (*asterisk*). Furthermore, in contrast to adult VillinCre^{ERT2};MYO5B$^{F/F}$ mice, VillinCre^{ERT2};MYO5B$^{F/F}$ neonates formed numerous internal ezrin-positive inclusions in the duodenum (*arrowheads*) that co-labeled with DPPIV. These inclusions resemble the microvillus inclusions found in in MYO5B KO and VillinCre;MYO5B$^{F/F}$ neonatal mice. *Scale bar*: 50 μm.

these gene-trap knockouts. With breeding onto the outbred CD1 strain, we were able to extend survival to approximately a week while preserving the MVID phenotype. Schneeberger et al[11] recently reported an inducible intestinally targeted MYO5B deletion mouse based on the VillinCre^{ERT2} driver and a fourth exon floxed allele. Many of the findings were similar to those we reported here, including induction of diarrhea, timing of loss of apical transporters, and alterations in apical and basolateral trafficking. Nevertheless, the report appears to differ from our findings on prevalence of microvillus inclusions after induction of MYO5B KO in adult mice. It seems likely that the numbers of inclusions in this previous investigation may have been overestimated because of a lack of comparison with either induction in neonatal mice or germline or constitutive KO mice. In addition, the absolute numbers of inclusions may vary in inducible mice based on strain differences and the exact time of induction vs the transition to adolescence after weaning, a time when one would expect to see a down-regulation of apical macropinocytosis owing to the cessation of breast feeding. The predominance of findings in our studies suggests that formation of microvillus inclusions in duodenal enterocytes is far more pronounced in neonates.

Our results in the MYO5B knockout strains also show that the manifestations of pathologic changes are region dependent. The previous reports in germline gene-trap and adult inducible MYO5B KO did not comment on regional differences within the small intestine.[10,11] As one might expect for a mechanism involved in apical internalization of maternal IgG, the microvillus inclusions in both germline and VillinCre;MYO5B$^{F/F}$ mice were predominant in the duodenum and proximal jejunum and essentially were absent in the ileum and colon. Previous investigations have noted microvillus inclusions are less frequent in the colonocytes of MVID patients.[28] In the germline and constitutive intestinal knockout mice, we also observed less prominent changes in apical transporters in the ileum. These findings indicate that the diarrheal phenotype may accrue predominantly from a duodenal deficit in absorption. Previous investigations have documented various differences in the physiology of duodenum, jejunum, and ileum.[29] Most notably, in studies of massive small-bowel resection, the ileum has a higher capacity to hypertrophy.[30] This phenomenon often is critical for the recovery of function in babies with short-gut syndrome.[31] If our findings in mice can be corroborated in children with MVID, then MVID diarrhea may be amenable to treatment with strategies for exclusion of the duodenum and promotion of ileal adaptation.

It is important to note that the MYO5B knockout mice did not recapitulate a number of the phenotypic changes usually associated with MVID.[9] First of all, we did not observe complete loss of microvilli in germline knockouts and VillinCre;MYO5B$^{F/F}$ mice. Rather these mice showed an intact brush border with short microvilli. These findings are in agreement with those in the MYO5B gene-trap KO model.[10] This microvillar phenotype is similar to that observed in Rab11a knockout mice.[17,18] Interestingly, in the tamoxifen-induced VillinCre^{ERT2};MYO5B$^{F/F}$ mice, we did observe microvillar denudation in some cells. A similar phenomenon also was reported by Schneeberger et al[11] in inducible MYO5B KO adult mice. Some of these differences may be owing to age-dependent observations. In the germline KO mouse models, observations were focused on mice in their first week of life, whereas the inducible mice essentially were adults. Similarly, human MVID children often do not undergo a biopsy until their third month of life. In addition, MVID children have usually spent weeks on total parenteral nutrition without luminal alimentation. A lack of luminal alimentation usually is associated with varying levels of villus atrophy.[32–34] Thus, the intestinal phenotype observed in MVID patients in their second or third month of life would reflect a combination of changes from the genetic disease along with the impact of extended bowel rest. We also did not observe the gross changes in junctional proteins such as E-cadherin in the germline and targeted knockout mice, so these more prominent losses in epithelial polarity observed in MVID children may reflect ramifications between disease and the lack of alimentation. Indeed, loss of E-cadherin was observed in a mouse model of total parenteral nutrition.[35] Alternatively, it is possible that dominant-negative mutations, such as the P660L MYO5B mutation in the Navajo, elicit a stronger phenotype than the knockout. The pathology in true human MYO5B knockouts has not been evaluated in depth. It also is notable that we did not observe any significant impact on the liver in germline knockouts. Similar results have been reported recently in the gene-trap MYO5B knockout mouse.[10] Liver disease in MVID patients has been noted previously as quite variable.[36] Early in vitro studies suggested that MYO5B was critical for proper assembly and function of the liver bile canaliculus.[37] However, liver disease in MVID patients may reflect an effect of extended parenteral nutrition from birth or a more subtle genetic deficit that is amplified in the presence of parenteral nutrition by MYO5B loss.

In summary, we have examined the effects of MYO5B loss in 3 separate mouse models reflecting germline deletion, constitutive intestinal deletion, and inducible intestinal deletion in both adults and neonates. Our findings show that microvillus inclusions are an indicator of MYO5B loss and likely reflect inhibition of recycling out of apical macropinosomes in the enterocytes of the proximal small intestine. Thus, this mutation has shown a previously unrecognized process operating in neonatal duodenal enterocytes. Nevertheless, our findings support the concept that the true pathology of the disease is manifested in the loss of proper trafficking and recycling of transporters to the apical brush border in enterocytes.[9,27] Our findings suggest that these apical transporters are diverted prominently to degradation pathways in the lysosome. Thus, treatment of MVID must focus on re-establishment of proper recycling, replacement of diseased enterocytes, or facilitation of mechanisms that still may be operable for distal intestine adaptation.

References

1. Erickson RP, Larson-Thome K, Valenzuela RK, et al. Navajo microvillous inclusion disease is due to a

mutation in MYO5B. Am J Med Genet A 2008; 146A:3117–3119.
2. Muller T, Hess MW, Schiefermeier N, et al. MYO5B mutations cause microvillus inclusion disease and disrupt epithelial cell polarity. Nat Genet 2008;40:1163–1165.
3. Ruemmele FM, Muller T, Schiefermeier N, et al. Loss-of-function of MYO5B is the main cause of microvillus inclusion disease: 15 novel mutations and a CaCo-2 RNAi cell model. Hum Mutat 2010;31:544–551.
4. Davidson GP, Cutz E, Hamilton JR, et al. Familial enteropathy: a syndrome of protracted diarrhea from birth, failure to thrive, and hypoplastic villus atrophy. Gastroenterology 1978;75:783–790.
5. Ruemmele FM, Schmitz J, Goulet O. Microvillous inclusion disease (microvillous atrophy). Orphanet J Rare Dis 2006;1:22.
6. Ameen NA, Salas PJ. Microvillus inclusion disease: a genetic defect affecting apical membrane protein traffic in intestinal epithelium. Traffic 2000;1:76–83.
7. Kravtsov D, Mashukova A, Forteza R, et al. Myosin 5b loss of function leads to defects in polarized signalling: implication for microvillus inclusion disease pathogenesis and treatment. Am J Physiol Gastrointest Liver Physiol 2014;307:G992–G1001.
8. Thoeni CE, Vogel GF, Tancevski I, et al. Microvillus inclusion disease: loss of myosin Vb disrupts intracellular traffic and cell polarity. Traffic 2013;15:22–42.
9. Knowles BC, Roland JT, Krishnan M, et al. Myosin Vb uncoupling from RAB8A and RAB11A elicits microvillus inclusion disease. J Clin Invest 2014;124:2947–2962.
10. Carton-Garcia F, Overeem AW, Nieto R, et al. Myo5b knockout mice as a model of microvillus inclusion disease. Sci Rep 2015;5:12312.
11. Schneeberger K, Vogel GF, Teunissen H, et al. An inducible mouse model for microvillus inclusion disease reveals a role for myosin Vb in apical and basolateral trafficking. Proc Natl Acad Sci U S A 2015; 112:12408–12413.
12. Lapierre LA, Avant KM, Caldwell CM, et al. Phosphorylation of Rab11-FIP2 regulates polarity in MDCK cells. Mol Biol Cell 2012;23:2302–2318.
13. Roland JT, Kenworthy AK, Peranen J, et al. Myosin Vb interacts with Rab8a on a tubular network containing EHD1 and EHD3. Mol Biol Cell 2007;18:2828–2837.
14. Dhekne HS, Hsiao NH, Roelofs P, et al. Myosin Vb and Rab11a regulate phosphorylation of ezrin in enterocytes. J Cell Sci 2014;127:1007–1017.
15. Saotome I, Curto M, McClatchey AI. Ezrin is essential for epithelial organization and villus morphogenesis in the developing intestine. Dev Cell 2004;6:855–864.
16. Groisman GM, Amar M, Livne E. CD10: a valuable tool for the light microscopic diagnosis of microvillous inclusion disease (familial microvillous atrophy). Am J Surg Pathol 2002;26:902–907.
17. Knowles BC, Weis VG, Yu S, et al. Rab11a regulates syntaxin 3 localization and microvillus assembly in enterocytes. J Cell Sci 2015;128:1617–1626.
18. Sobajima T, Yoshimura S, Iwano T, et al. Rab11a is required for apical protein localisation in the intestine. Biol Open 2014;4:86–94.
19. Jones EA, Waldmann TA. The mechanism of intestinal uptake and transcellular transport of IgG in the neonatal rat. J Clin Invest 1972;51:2916–2927.
20. Israel EJ, Taylor S, Wu Z, et al. Expression of the neonatal Fc receptor, FcRn, on human intestinal epithelial cells. Immunology 1997;92:69–74.
21. Simister NE, Mostov KE. An Fc receptor structurally related to MHC class I antigens. Nature 1989; 337:184–187.
22. Bry L, Falk P, Huttner K, et al. Paneth cell differentiation in the developing intestine of normal and transgenic mice. Proc Natl Acad Sci U S A 1994;91: 10335–10339.
23. Shah U, Dickinson BL, Blumberg RS, et al. Distribution of the IgG Fc receptor, FcRn, in the human fetal intestine. Pediatr Res 2003;53:295–301.
24. Rodewald R. Intestinal transport of antibodies in the newborn rat. J Cell Biol 1973;58:189–211.
25. He W, Ladinsky MS, Huey-Tubman KE, et al. FcRn-mediated antibody transport across epithelial cells revealed by electron tomography. Nature 2008; 455:542–546.
26. Sato K, Nagai J, Mitsui N, et al. Effects of endocytosis inhibitors on internalization of human IgG by Caco-2 human intestinal epithelial cells. Life Sci 2009; 85:800–807.
27. Vogel GF, Klee KM, Janecke AR, et al. Cargo-selective apical exocytosis in epithelial cells is conducted by Myo5B, Slp4a, Vamp7, and Syntaxin 3. J Cell Biol 2015; 211:587–604.
28. Phillips AD, Jenkins P, Raafat F, et al. Congenital microvillous atrophy: specific diagnostic features. Arch Dis Child 1985;60:135–140.
29. James PS, Smith MW, Tivey DR. Single-villus analysis of disaccharidase expression by different regions of the mouse intestine. J Physiol 1988;401:533–545.
30. Dowling RH, Booth CC. Structural and functional changes following small intestinal resection in the rat. Clin Sci 1967;32:139–149.
31. Tappenden KA. Mechanisms of enteral nutrient-enhanced intestinal adaptation. Gastroenterology 2006; 130:S93–S99.
32. Sun X, Spencer AU, Yang H, et al. Impact of caloric intake on parenteral nutrition-associated intestinal morphology and mucosal barrier function. JPEN J Parenter Enteral Nutr 2006;30:474–479.
33. Sakamoto K, Hirose H, Onizuka A, et al. Quantitative study of changes in intestinal morphology and mucus gel on total parenteral nutrition in rats. J Surg Res 2000; 94:99–106.
34. Buchman AL, Moukarzel AA, Bhuta S, et al. Parenteral nutrition is associated with intestinal morphologic and functional changes in humans. JPEN J Parenter Enteral Nutr 1995;19:453–460.
35. Feng Y, Sun X, Yang H, et al. Dissociation of E-cadherin and beta-catenin in a mouse model of total parenteral nutrition: a mechanism for the loss of epithelial cell proliferation and villus atrophy. J Physiol 2009;587:641–654.
36. Girard M, Lacaille F, Verkarre V, et al. MYO5B and bile salt export pump contribute to cholestatic liver disorder

in microvillous inclusion disease. Hepatology 2014; 60:301–310.

37. Wakabayashi Y, Dutt P, Lippincott-Schwartz J, et al. Rab11a and myosin Vb are required for bile canalicular formation in WIF-B9 cells. Proc Natl Acad Sci U S A 2005;102:15087–15092.

Received October 16, 2015. Accepted November 25, 2015.

Correspondence
Address correspondence to: James R. Goldenring, MD, PhD, Epithelial BIology Center, Vanderbilt University Medical Center, 10435 Medical Research Building IV, 2213 Garland Avenue, Nashville, Tennessee 37232. e-mail: jim.goldenring@vanderbilt.edu; fax: (615) 343-1591.

Conflicts of interest
The authors disclose no conflicts.

Funding
Supported by the National Institutes of Health RO1 grants DK70856 and DK48370 (J.R.G.), and by T32 DK007673 (V.G.W.). Confocal and structured illumination fluorescence microscopy as well as transmission electron microscopy and scanning electron microscopy imaging was performed through the use of the Vanderbilt University Medical Center Cell Imaging Shared Resource and histologic sectioning was performed by Translational Pathology Shared Resource, both of which are supported by National Institutes of Health grants CA68485, DK20593, DK58404, and HD15052. Mouse models were developed in the Shared Resources of the Vanderbilt Stem Cell Center, which is supported by National Institutes of Health grant CA68485. Fluorescence slide imaging was performed on an Ariol SL-50 digitizing scanner (Applied Imaging/ Leca, Vista, CA) in the Vanderbilt University Medical Center Digital Histology Shared Resource.